

PHASE-FIELD MODELING OF TWO PHASE FLUID FILLED FRACTURES IN A POREOELASTIC MEDIUM*

SANGHYUN LEE[†], ANDRO MIKELIĆ[‡], MARY F. WHEELER[§], AND THOMAS WICK[¶]

Abstract. We propose an immiscible two phase flow fracture model, based on a phase-field for treating crack propagation in porous media. This multifluid model is an extension of classical flow models and we take into account nonzero capillary pressure. Using lubrication theory, we provide details of the determination of effective parameters: absolute and relative permeabilities. The phase-field formulation is a generalization of previous works by the authors and extends the single phase model to the two phase case. Here the resulting flow system has four unknowns: resident and injected pressures and saturations, respectively. The solid contribution consists of displacements and a phase-field variable. Both systems are coupled employing a fixed-stress splitting. Therein, the flow problem is treated with an iterative scheme and the solid problem fully implicitly. Modeling and algorithms are substantiated with several numerical tests.

Key words. finite elements, phase-field fracture, Biot system, fixed-stress iterative coupling, multiphase flow, fracture propagation

AMS subject classifications. 74F10, 74S05, 76S05, 35Q86, 74A45

DOI. 10.1137/17M1145239

1. Introduction. Coupled multiphase fluid flow and deformation in fractured porous rock are important in energy and environmental applications. Hydraulic fracturing and horizontal drilling are considered to be the major reasons the U.S. has been having an energy revolution, one that has changed the energy picture from scarcity to abundance. Fracking, the forcing opening of fissures in subsurface rocks by introducing liquid at high pressure, is letting the U.S. tap vast oil and natural gas reserves that previously were locked away in shale and other tight-rock formations. Up to 95 percent of natural gas wells drilled in the next decade will utilize hydraulic fracturing [33] and by 2040, over 80 percent of U.S. natural gas production is projected to come from formations that need to be hydraulically fractured to be accessible [1]. Additional important examples involving subsurface fluid structure interactions include geothermal energy production, deep underground injection of hazardous wastes, and storage of carbon sequestration into saline aquifers and depleted oil and gas reservoirs.

*Received by the editors August 28, 2017; accepted for publication (in revised form) July 16, 2018; published electronically October 9, 2018.

<http://www.siam.org/journals/mms/16-4/M114523.html>

Funding: The research of the first and third authors was partially supported by Center for Frontiers of Subsurface Energy Security, an Energy Frontier Research Center funded by the U.S. Department of Energy, Office of Science, and Office of Basic Energy Sciences, DOE Project DE-SC0001114, and a DOE grant DE FG02-04ER25617. The third author was also partially supported by Moncrief Grand Challenge Faculty Awards from The Institute for Computational Engineering and Sciences (ICES), the University of Texas at Austin. The second and fourth authors were supported by The J. Tinsley Oden Faculty Fellowship Research Program and Center for Subsurface Modeling at Institute for Computational Engineering and Science (ICES), the University of Texas at Austin.

[†]Department of Mathematics, Florida State University, 1017 Academic Way, Tallahassee, FL 32306 (lee@math.fsu.edu).

[‡]Univ Lyon, Université Claude Bernard Lyon 1, CNRS UMR 5208, Institut Camille Jordan, 43, blvd. du 11 novembre 1918, 69622 Villeurbanne Cedex, France (Andro.Mikelic@univ-lyon1.fr).

[§]Center for Subsurface Modeling, The Institute for Computational Engineering and Sciences, The University of Texas at Austin, Austin, TX 78712 (mfw@ticam.utexas.edu).

[¶]Institut für Angewandte Mathematik, Leibniz Universität Hannover, Welfengarten 1, 30167 Hannover, Germany (thomas.wick@ifam.uni-hannover.de).

The latter has been considered to be a major technology for reducing the emission of greenhouse gases to the atmosphere.

Numerical simulations are essential in understanding the performance of the above coupled systems in a highly complex heterogeneous porous media with multiple temporal and spatial scales. For example modeling hydraulic fracturing requires three dimensional compositional fluid models, multiphase, thermal, proppant transport with gravitational settling, water solute transport, and includes quasi-Newtonian fluid rheology with modified power law coupled with a geomechanics elasticity model that can treat fracture propagation. These simulator capabilities enable comparison of proposed fracturing designs for predicted production and refracturing near depleted wells and optimization designs for slick water injection and possible usage of other fracturing fluids such as CO₂ and foam. Strategies for carbon sequestration and geothermal production utilize similar mathematical models and numerical simulators. These numerical studies are important in addressing environmentally prudent procedures.

There is a long list of environmental issues that need to be considered such as groundwater contamination and surface water pollution. In addition to water quality issues, fracking wells release compounds into the air, such as benzene, ethylbenzene, toluene, and n-hexane; long-term exposure to these has been linked to birth defects, neurological problems, and blood disorders. In addition many areas of the United States, not considered earthquake prone, such as Texas and Oklahoma, are now experiencing relatively strong seismic activity. In 2015, an area of North Texas had nine confirmed earthquakes in a 24-hour period. Fracking is being investigated as the cause; hence, a quantitative understanding of fracking is crucial.

There has been considerable research in modeling fluid flow in a fractured porous media going back to the 1960s with the development of the Perkins–Kern–Nordgren model [74, 81] and the Khristianovich–Geertsma–de Klerk model [100]. These two dimensional models assumed fractures with constant height and differed primarily because of the assumption of plane strain in the vertical and horizontal directions, respectively. In recent years, a common practice has been the linking of simulators, each specialized to flow or mechanics, as in the case of TOUGH2 and FLAC3D [82]. For more details regarding the coupling between fracture geometry and fluid flow problems, the reader is referred to [2, 31]. Recently, several other approaches have been discussed in [27, 30, 37–39, 48, 59, 71, 73, 78, 86].

The authors have been involved in the development of high fidelity phase-field models for fracture propagation in a poroelastic medium. Recent advances and numerical studies for treating multiphysics phase-field fractures include the following; thermal shocks and thermo-elastic-plastic solids [18, 61, 63], elastic gelatin for wing crack formation [53], pressurized fractures [17, 67, 69, 94, 95, 97], fluid filled (i.e., hydraulic) fractures [40, 54, 55, 58, 60, 62, 68, 98], proppant-filled fractures [52], variably saturated porous media [21], and crack initiations with microseismic probability maps [57]. These computational examples demonstrate the potential of phase-field for fracture propagation.

Phase-field is a regularized approach that clearly has advantages and shortcomings. A list from the authors' experience is as follows. The first advantage is a continuum description based on first physical principles to determine the unknown crack path [36] and the computation of curvilinear and complex crack patterns. The model allows for nucleation, branching, and merging and postprocessing of certain quantities such as stress intensity factors becomes redundant. Therefore, easy handling of fracture networks in possibly highly heterogeneous media can be treated.

The formulation being described in a variational framework allows finite element discretizations and corresponding analyses. Phase-field is a fixed-mesh approach in which no remeshing or update of basis functions to resolve the crack path is needed. The mathematical model permits any dimension $d = 2, 3$, and in case the software allows as well, phase-field fracture applies conveniently to three dimensional simulations. On the energy level, the formulation is nonconvex constituting a challenge for both theory and design of numerical algorithms. A second challenge is the computational cost since either additional iterations in an alternating approach [15] are required or a fully nonlinear problem has to be solved. However, our quasi-monolithic approach [41, 54] has low Newton iteration numbers and therein the major cost goes into solving the vector-valued elasticity problem that also applies using most other crack models (such as extended/generalized finite elements for instance). Two bigger downsides are the accurate crack width computations (despite that some recent ideas have been proposed [56, 72]), and also the smeared fracture transition zone when additional physics (a given pressure, proppant, or saturations as in the current paper) shall be described in, or around, the fracture or on the fracture boundary. Here, local mesh adaptivity helps to a great extent in order to achieve sufficient accuracy. As demonstrated in our own work and by others (see the references in the previous paragraph), ideas have been proposed of how to cope with these challenges. In view of the increasing popularity, it however seems that the advantages outweigh the shortcomings for today's applications.

In this paper, we are specifically interested in extending our porous media phase-field fracture model to two phase flow inside the fracture. While two phase flow for nonfractured media is well established [9, 23, 80], the extension to fractures that are propagating is a challenge. The novelties in the development of our two phase flow model for a propagating fracture is based on two steps. First, using lubrication theory, we compute the absolute and relative permeabilities. In the second step, these quantities are substituted into the full three dimensional equations for two phase flow.

With regard to numerical modeling, we finally need to solve four problems: a nonlinear displacement/phase-field system, a pressure system, a saturation equation, and a crack width problem. Here, the two important aspects in question are the coupling algorithm and discretization schemes with appropriate conservation properties. For the displacement/phase-field fracture subproblem, we employ a quasi-monolithic approach [41, 54, 96]. To couple this fractured-geomechanics problem to flow, we use a splitting method. The numerical discretization in space is based on continuous Galerkin finite elements for displacements and phase-field, and an enriched Galerkin finite element approach [50, 51, 88] is applied for both the pressure and saturation equations in order to obtain local mass conservation with an efficient solver.

The outline of this paper is as follows: In section 2, we briefly recapitulate phase-field modeling of hydraulic fractures in porous media and a width computation. Section 3 presents the derivation of a two phase flow model for propagating fractures; we discuss the single phase flow model for a reservoir in section 4. In section 5, we present the global solution algorithm and explain variational formulations and finite element discretization including decomposition of the fracture and reservoir domain as a diffraction system. In the short section 6, we briefly describe the numerical solvers and emphasize the importance of local mesh refinement. Several numerical examples are provided in section 7. A summary of our results is given in the conclusions in section 8.

2. Modeling phase-field fracture in a porous medium. We now recapitulate the essentials for phase-field modeling for pressurized and fluid filled fractures in porous media, as described in [54, 69, 70].

We seek a vector-valued displacement $\mathbf{u}(\cdot, t) : \Lambda \times (0; T) \rightarrow \mathbb{R}^d (d \in \{2, 3\})$, a scalar-valued pressure $p(\cdot, t) : \Lambda \times (0; T) \rightarrow \mathbb{R}$, and a scalar-valued phase-field function (namely, a smoothed indicator function) $\varphi(\cdot, t) : \Lambda \times (0; T) \rightarrow [0, 1]$, which will satisfy the equations of the model in the weak sense. In order to satisfy the initial conditions, the above functions are considered as Hilbert space valued functions, defined on $[0, T]$. They take values in appropriate Sobolev spaces with respect to the spatial variable. Furthermore, $\Omega_F(t)$ is an open and connected set corresponding to the fracture and $\Omega_R(t)$ is an open and connected set corresponding to the unbroken material for every $t \in [0, T]$. The phase-field is a smoothed indicator function of $\Omega_R(t)$. Here, $\Lambda = \Omega_F \cup \Omega_R \cup \Gamma_F$ is the entire domain and $\Gamma_F = \overline{\Omega}_F \cap \overline{\Omega}_R$ is the fracture boundary. The boundary $\partial\Lambda$ splits into a Dirichlet part $\partial_D\Lambda$ and a Neumann part $\partial_N\Lambda$.

2.1. Constitutive laws in the reservoir. The solid displacements and diffusive flow in a nonfractured porous medium are modeled in Ω_R by the classical quasi-static elliptic-parabolic Biot system for a porous solid saturated with a slightly compressible viscous fluid. Let $p_R = p|_{\Omega_R}$ be the pressure in the reservoir and $p_F = p|_{\Omega_F}$ be the pressure in the fracture. The constitutive equation for the Cauchy stress tensor is given as

$$(2.1) \quad \sigma^{por}(\mathbf{u}, p_R) - \sigma_0 = \sigma_R(\mathbf{u}) - \alpha(p_R - p_0)\mathbf{I} \quad \text{in } \Omega_R \times (0, T),$$

where \mathbf{u} is the displacement, p_0 is the initial reservoir pressure, \mathbf{I} is the identity tensor, σ_0 is the initial stress value, and $\alpha \in [0, 1]$ is Biot's coefficient. The effective linear elastic stress tensor is

$$(2.2) \quad \sigma_R := \sigma|_{\Omega_R} = \sigma_R(\mathbf{u}) := \lambda(\nabla \cdot \mathbf{u})\mathbf{I} + 2Ge(\mathbf{u}),$$

where $\lambda, G > 0$ are the Lamé coefficients. The linear elastic strain tensor is given as $e(\mathbf{u}) := \frac{1}{2}(\nabla \mathbf{u} + \nabla \mathbf{u}^T)$. Then the balance of linear momentum in the solid reads

$$(2.3) \quad -\nabla \cdot \sigma^{por}(\mathbf{u}, p_R) = \rho_s \mathbf{g} \quad \text{in } \Omega_R \times (0, T),$$

where ρ_s is the density of the reservoir solid and \mathbf{g} is the gravity. For simplicity in this paper, we assume homogeneous Dirichlet boundary conditions on $\partial\Lambda$ for the displacement \mathbf{u} .

2.2. A quasi-static phase-field model for pressurized fractures. As in the variational setting for linear elasticity in [16], our phase-field formulation utilizes the elliptic (Ambrosio–Tortorelli) functional [5, 6]. In the following, we recapitulate our phase-field fracture approach for pressurized and fluid filled fractures in porous media as established in [67–69]. Here, we assume that the fracture is a three dimensional thin object where the width is much smaller than the length, and where the leading order of the fracture fluid stress is derived from lubrication theory.

The effective fluid stress is given by $\sigma_F := \sigma|_{\Omega_F} = -p_F\mathbf{I}$. As transmission conditions, we assume continuity of normal stresses:

$$\sigma^{por} \cdot \mathbf{n}_F = \sigma_F \cdot \mathbf{n}_F \quad \text{on } \Gamma_F \times (0, T)$$

or

$$(2.4) \quad (\sigma_R(\mathbf{u}) - \alpha p_R \mathbf{I}) \cdot \mathbf{n}_F = -p_F \mathbf{n}_F \quad \text{on } \Gamma_F \times (0, T),$$

where $\Gamma_F := \overline{\Omega}_R \cap \overline{\Omega}_F$ is the fracture interface (crack surface) and \mathbf{n}_F is the outward pointing normal vector on Γ_F . In the following we use the second transmission condition, namely, continuity of pressures

$$(2.5) \quad p_R = p_F \quad \text{on } \Gamma_F \times (0, T).$$

Consequently we identify $p_R = p_F = p$ and obtain:

$$(2.6) \quad (\sigma_R(\mathbf{u}) - \alpha p I) \cdot \mathbf{n}_F = -p \mathbf{n}_F \quad \text{on } \Gamma_F \times (0, T).$$

Next, we follow [7] in which the stress tensor σ is additively decomposed as

$$\sigma = \sigma_R = \sigma^+(\mathbf{u}) + \sigma^-(\mathbf{u})$$

into a tensile part $\sigma^+(\mathbf{u})$ and a compressive part $\sigma^-(\mathbf{u})$ by

$$(2.7) \quad \sigma^+(\mathbf{u}) := \left(\frac{2}{d} G + \lambda \right) \text{tr}^+(e(\mathbf{u})) I + 2G(e(\mathbf{u}) - \frac{1}{d} \text{tr}(e(\mathbf{u})) I),$$

$$(2.8) \quad \sigma^-(\mathbf{u}) := \left(\frac{2}{d} G + \lambda \right) \text{tr}^-(e(\mathbf{u})) I,$$

and

$$(2.9) \quad \text{tr}^+(e(\mathbf{u})) = \max(\text{tr}(e(\mathbf{u})), 0), \quad \text{tr}^-(e(\mathbf{u})) = \text{tr}(e(\mathbf{u})) - \text{tr}^+(e(\mathbf{u})).$$

We notice that however the influence of different energy/stress splitting laws is still a subject of discussion in the fracture mechanics community (see [4] and section 2.2 in [14]). Moreover, pressurized fractures are basically subject to tension forces in which the splitting into σ^+ and σ^- becomes redundant; see section 5.2 in [69].

By applying (2.6) and Gauss' divergence theorem (see section 3.2 in [70]), the strong Euler–Lagrange Formulation 1 for a quasi-static model of a pressurized phase-field fracture is described below. By utilizing the definition of φ and the interface conditions, namely (2.5) and (2.6), we do not distinguish between σ_R, p_R and σ_F, p_F in the global dissipation form.

FORMULATION 1 (pressurized displacement phase-field fracture). *Let the phase-field regularization parameters be $\varepsilon > 0$ and $\kappa > 0$ with $\kappa \ll \varepsilon$. Here ε is the length of a smooth phase-field transition zone where $\varphi \in (0, 1)$; we refer to Figure 5 for details. Given a pressure p and a phase-field φ , find displacements \mathbf{u} such that*

$$\begin{aligned} -\nabla \cdot (((1 - \kappa)\varphi^2 + \kappa)\sigma^+) - \nabla \cdot \sigma^- + \varphi^2 \nabla p + (\alpha - 1)\nabla(\varphi^2 p) &= 0 \quad \text{in } (0, T) \times \Lambda, \\ \mathbf{u} &= 0 \quad \text{on } (0, T) \times \partial_D \Lambda. \end{aligned}$$

Similarly, given displacements \mathbf{u} and given a pressure p , find a phase-field variable φ such that

$$\begin{aligned} \left(-G_c \varepsilon \Delta \varphi - \frac{G_c}{\varepsilon} (1 - \varphi) + (1 - \kappa)\sigma^+ : e(\mathbf{u}) \varphi \right. \\ \left. + 2(1 - \alpha)\varphi p (\nabla \cdot \mathbf{u}) + 2\varphi \nabla p \cdot \mathbf{u} \right) \partial_t \varphi &= 0 \quad \text{in } (0, T) \times \Lambda, \\ \frac{\partial \varphi}{\partial \mathbf{n}} &= 0 \quad \text{on } (0, T) \times \partial \Lambda, \\ \varphi(0) &= \varphi^0 \quad \text{in } \{t = 0\} \times \Lambda, \end{aligned}$$

where \mathbf{n} is the outward pointing normal vector on $\partial\Lambda$ and $G_c > 0$ is the energy release rate. In addition, the phase-field variable is subject to an irreversibility constraint and yields an inequality system including a compatibility condition

$$\begin{aligned} -G_c\varepsilon\Delta\varphi - \frac{G_c}{\varepsilon}(1-\varphi) + (1-\kappa)\sigma^+ : e(\mathbf{u})\varphi \\ + 2(1-\alpha)\varphi p\nabla \cdot \mathbf{u} + 2\varphi\nabla p \cdot \mathbf{u} \leq 0 \quad \text{in } (0, T) \times \Lambda, \\ \partial_t\varphi \leq 0 \quad \text{in } (0, T) \times \Lambda, \end{aligned}$$

which is frequently referred as a Rice condition. Moreover, in the discretized system, we also require $h_K \ll \varepsilon$, where h_K is the local discretization parameter.

Remark 2.1. Because the displacement equations are quasi-static, without explicit time dependence, the displacement value at $t = 0$ can be computed with φ^0 and $p|_{t=0}$.

2.3. Computation of the fracture width. In the displacement phase-field system, the width of the fracture is not explicitly defined. For accurate width computations of nonplanar fractures an additional algorithm is required. Formally the definition of the width reads

$$2w := 2w(\mathbf{u}) = 2h = -[\mathbf{u} \cdot \mathbf{n}_F],$$

which is the jump of the normal displacements, where \mathbf{n}_F is the unit normal on the crack surface (Γ_F). For the meaning of h , we refer the reader to Figure 1.

Using explicitly the phase-field variable, this definition can be rewritten as

$$2w = -[\mathbf{u} \cdot \mathbf{n}_F] = -2\mathbf{u} \cdot \frac{\nabla\varphi_{LS}}{\|\nabla\varphi_{LS}\|}$$

by approximating the normal vector on the crack surface (Γ_F) with the level set values φ_{LS} of a specific isoline of the fracture. To compute φ_{LS} , we proceed as follows: Let Γ_F be the fracture interface. We now define Γ_F as the zero level set of a function φ_{LS} such that

$$\begin{aligned} \varphi_{LS} &> 0, & \mathbf{x} \in \Omega_R, \\ \varphi_{LS} &< 0, & \mathbf{x} \in \Omega_F, \\ \varphi_{LS} &= 0, & \mathbf{x} \in \Gamma_F, \end{aligned}$$

where the isoline φ_{LS} is obtained from the phase-field variable φ by

$$(2.10) \quad \varphi_{LS} := \varphi - C_{LS}.$$

Here, $C_{LS} \in (0, 1)$ is a constant selected for approximating the fracture boundary Γ_F . Throughout this paper for simplicity, we set $C_{LS} = 0.1$. Thus, we have $\Gamma_F := \{\mathbf{x} \in \Lambda \mid \varphi(\mathbf{x}, t) = C_{LS}\}$, $\Omega_R := \{\mathbf{x} \in \Lambda \mid \varphi(\mathbf{x}, t) > C_{LS}\}$, and $\Omega_F := \{\mathbf{x} \in \Lambda \mid \varphi(\mathbf{x}, t) < C_{LS}\}$. Details of the entire procedure and underlying motivation are provided in [56, 72].

Remark 2.2. In order to improve the fracture width representation inside the fracture, we finally solve a crack width interpolation problem; see [56, Formulation 6 and Figure 4]). We omit the continuous problem statement here, but we directly provide the Galerkin approximation in Formulation 6.

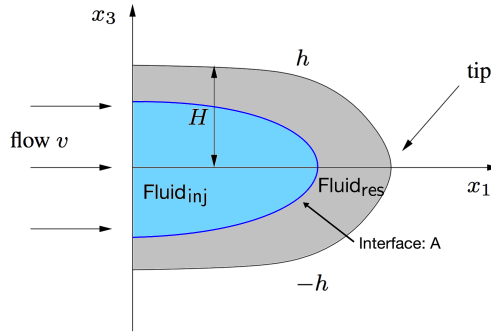


FIG. 1. Sketch of the near-tip fracture region for a two dimensional setting. $Fluid_{res}$ is the residing fluid in the domain and $Fluid_{inj}$ is injected from a source in the fracture. $p_{F,res}$ and $p_{F,inj}$ are the corresponding pressure values. The interface A is defined between the two fluids. Fracture boundary $x_3 = \pm h(x_1, x_2, t)$ moves in time. We assume that the characteristic width H of the fracture is much bigger than the pore size of the porous medium. We recall that for $H = c_0 l^{2/3}$, where l is the pore size, a coupled model must be taken into account. In three dimensions, the x_2 coordinate goes into the plane and the one dimensional curve $h(x_1, x_2, t)$ becomes a two dimensional surface. We finally notice that $H = c_0 l^{(2/3)}$ is a kind of threshold value. If H is smaller than that value then the effective filtration does not see the fracture. If H is bigger than the threshold value then one has to couple two adjacent domains; see [19].

3. Modeling two phase flow in a fracture. We concentrate now on a detailed derivation of a two phase flow model inside a propagating fracture. A characteristic situation is illustrated in Figure 1. An important aspect is to formulate a novel model with the surrounding reservoir. The goal is to derive a two dimensional pressure-saturation system from which we extract absolute and relative permeabilities and capillary pressure. These quantities are then used in a standard three dimensional two phase flow system. To this end, we develop a lubrication model that not only computes p_F but also the saturation and provides an explicit computation of the relative permeabilities. Our model is derived from first principle laws and results via upscaling into a three dimensional lubrication model. Finally, we use a physically based phenomenological constitutive law to account for the capillary pressure.

3.1. A model for a two phase flow in a flat symmetric three dimensional (3D) penny shape fracture. In the following, we derive a model for two phase flow in a fracture that includes explicitly computed absolute and relative permeabilities. To this end, we start from first principles by working with the multifluid Stokes equations. For the fracture geometry we assume a flat 3D fracture occupying the domain Ω_F and which is characterized by the ratio ε between its characteristic width H in the direction x_3 and its characteristic horizontal length L in directions x_1 and x_2 ; a sketch is provided in Figure 1.

3.1.1. Coupling conditions and a two phase flow Stokes model. Our first assumption is that the crack boundary propagates in a deformable porous medium. This boundary can be described as

$$(3.1) \quad x_3 = h(x_1, x_2, t) \quad \text{for } x_3 \geq 0 \quad \text{and} \quad x_3 = -h(x_1, x_2, t) \quad \text{for } x_3 < 0.$$

The so-called tip region is defined where h and $-h$ meet at $x_3 = 0$. We further assume that the fluid flow in the fracture is given by the incompressible Navier-Stokes equations for two immiscible viscous fluids (see, e.g., [91]). The second fluid

is being injected through an injection well in the middle of the crack and pushes the residing fluid. Between these two immiscible fluids, we introduce a free boundary $x_3 = A(x_1, x_2, t)$ (i.e., the interface). On the interface A we deal with the usual transmission conditions:

- continuity of the velocities;
- continuity of normal stresses.

Remark 3.1 (surface tension). Initially, we neglect the surface tension. These effects will be taken into account later via energy interface considerations.

Since we assume two immiscible fluids, we have a third condition on the interface A . Let \mathbf{v} be the fluid velocity, then

$$(3.2) \quad \frac{DA}{Dt} - v_3|_{x_3=A} = \frac{\partial A}{\partial t} - v_3|_{x_3=A} + (v_1, v_2)|_{x_3=A} \cdot \nabla_{x_1, x_2} A = 0.$$

To derive a two phase flow model, classically one would distinguish the two flow equations. We utilize the work of Demay, Nouri and Poupaud in [75, 76], who formulated a model, which assumes that the transmission and nonmiscibility conditions at the interface follow from the global formulation of a linear transport equation for the viscosity. Furthermore, the momentum and mass conservation conditions are described by the standard (linear) Stokes equations. Consequently, our two fluid system has the form find \mathbf{v}, p, η such that

$$(3.3) \quad \nabla p - \nabla \cdot (2\eta e(\mathbf{v})) = 0 \quad \text{in } \Omega_F \times (0, T),$$

$$(3.4) \quad \nabla \cdot \mathbf{v} = q \quad \text{in } \Omega_F \times (0, T),$$

$$(3.5) \quad \frac{\partial \eta}{\partial t} + \nabla \cdot (\eta \mathbf{v}) = q\eta \quad \text{in } \Omega_F \times (0, T),$$

$$(3.6) \quad \eta|_{t=0} = \eta_0(x) \quad \text{in } \Omega_F \times (0, T),$$

where q is a source term, v is the velocity, p is the fluid pressure, $e(\mathbf{v})$ is the rate-of-strain tensor, and η is the viscosity. Specifically, the viscosity can only take two values, i.e., $\eta \in \{\eta_{F,\text{res}}, \eta_{F,\text{inj}}\}$, where $\eta_{F,\text{res}}$ and $\eta_{F,\text{inj}}$ are the residing and injecting viscosities, respectively. We notice that the flow equations are given in the entire domain Ω_F and to determine the specific phase is achieved with the help of (3.6).

3.1.2. A rescaled Stokes system in a penny-shaped geometry. Next, we derive a dimensionless form of the lubrication equation corresponding to a displacement of the fracture fluid by a radial source injection following the classical lubrication theory references (see, e.g., [90]). For the channel and tube flow, such equations were derived in [35, 64]. Here we consider a penny-shaped fracture. We will follow the two scaled expansions introduced in [64].

Let U be the characteristic velocity in the directions x_1 and x_2 and $\mathbf{Re} = UL/\eta_{F,\text{res}}$ is the Reynolds number. We assume that \mathbf{Re} is small, which justifies using the Stokes equation ((3.3) and (3.4)) instead of the full Navier–Stokes equations.

Next, we set the characteristic quantities

$$\begin{aligned} \bar{t} &= \frac{U}{L}t, & x &= \frac{x_1}{L}, & y &= \frac{x_2}{L}, & z &= \frac{x_3}{H}, & v_x &= \frac{v_1}{U}, & v_y &= \frac{v_2}{U}, & v_z &= \frac{v_3 L}{U H}, \\ a &= \frac{A}{H}, & \bar{p} &= \frac{H^2}{\eta_{F,\text{res}} L U} p, & w(x, y, \bar{t}) &= \frac{1}{H} h(x_1, x_2, t), & \bar{q} &= \frac{q L}{U}, \\ \varepsilon &= \frac{H}{L}, & \omega &= \frac{\Omega_F}{L}, & \eta^\varepsilon &= \frac{\eta}{\eta_{F,\text{res}}}, & M &= \frac{\eta_{F,\text{inj}}}{\eta_{F,\text{res}}}. \end{aligned}$$

We remark that the ε in this section is not linked to the phase-field regularization parameter. For simplicity, we skip the bars in the following and denote the rescaled $\Omega_F = \omega \times (-h, h)$ with the same symbol. In addition, we add the index ε to the unknowns, to indicate that the system under consideration contains a small parameter.

With these preliminaries, the system (3.3)–(3.6) can be rewritten as

$$(3.7) \quad -\partial_x p^\varepsilon + \partial_z (\eta^\varepsilon \partial_z v_x^\varepsilon) + O(\varepsilon^2) = 0 \quad \text{in } \Omega_F,$$

$$(3.8) \quad -\partial_y p^\varepsilon + \partial_z (\eta^\varepsilon \partial_z v_y^\varepsilon) + O(\varepsilon^2) = 0 \quad \text{in } \Omega_F,$$

$$(3.9) \quad -\partial_z p^\varepsilon + O(\varepsilon^2) = 0 \quad \text{in } \Omega_F,$$

$$(3.10) \quad \partial_x v_x^\varepsilon + \partial_y v_y^\varepsilon + \partial_z v_z^\varepsilon = \bar{q} \quad \text{in } \Omega_F,$$

$$(3.11) \quad \partial_t \eta^\varepsilon + \partial_x (\eta^\varepsilon v_x^\varepsilon) + \partial_y (\eta^\varepsilon v_y^\varepsilon) + \partial_z (\eta^\varepsilon v_z^\varepsilon) = \bar{q} \eta^\varepsilon \quad \text{in } \Omega_F.$$

Our main assumption is that $\text{Fluid}_{\text{res}}$ is already present in the fracture (and also in the reservoir) and that the injected fluid does not reach the fracture boundary:

$$\eta^\varepsilon|_{t=0} = M \chi_{\{-a_0(x_1, x_2) \leq z \leq a_0(x_1, x_2)\}} + \chi_{\{-w \leq z < -a_0(x_1, x_2) \text{ and } a_0(x_1, x_2) < z \leq w\}},$$

$$(3.12) \quad \text{supp } \bar{q} \subset \{-a_0(x_1, x_2) \leq z \leq a_0(x_1, x_2)\},$$

where $a_0 \geq 0$ is a smooth surface with compact support in Ω_F .

3.1.3. Normal and tangential vectors. We recall that the unit normal \mathbf{n} and tangential vectors $\boldsymbol{\tau}^{(j)}$, $j = 1, 2$, can be expressed in the form

$$\mathbf{n} = \frac{-\varepsilon \partial_x w \mathbf{e}^1 - \varepsilon \partial_y w \mathbf{e}^2 + \mathbf{e}^3}{\sqrt{1 + \varepsilon^2 |\nabla_{x,y} w|^2}}, \quad \boldsymbol{\tau}^{(1)} = \frac{\mathbf{e}^1 + \varepsilon \partial_x w \mathbf{e}^3}{\sqrt{1 + \varepsilon^2 |\partial_x w|^2}}, \quad \boldsymbol{\tau}^{(2)} = \frac{\mathbf{e}^2 + \varepsilon \partial_y w \mathbf{e}^3}{\sqrt{1 + \varepsilon^2 |\partial_y w|^2}}.$$

Then for $v = U(v_x^\varepsilon, v_y^\varepsilon, v_z^\varepsilon)$ we have

$$\mathbf{v} \cdot \mathbf{n} = \frac{-U\varepsilon \partial_x w v_x^\varepsilon - U\varepsilon \partial_y w v_y^\varepsilon + U\varepsilon v_z^\varepsilon}{\sqrt{1 + \varepsilon^2 |\nabla_{x,y} w|^2}} = U\varepsilon (v_z^\varepsilon - \nabla_{x,y} w \cdot (v_x^\varepsilon, v_y^\varepsilon)) + O(\varepsilon^3),$$

$$\mathbf{v} \cdot \boldsymbol{\tau}^{(1)} = \frac{U v_x^\varepsilon + U \varepsilon \partial_x w v_z^\varepsilon}{\sqrt{1 + \varepsilon^2 |\partial_x w|^2}} = U v_x^\varepsilon + U \varepsilon \left(\partial_x w v_z^\varepsilon - \varepsilon \frac{v_x^\varepsilon}{2} (\partial_x w)^2 \right) + O(\varepsilon^3),$$

and analogously for $\mathbf{v} \cdot \boldsymbol{\tau}^{(2)}$. The velocity in the fracture is larger than in the surrounding porous medium. Hence we have on the boundary $z = w(x, y, t)$,

$$(3.13) \quad 0 = \mathbf{v} \cdot \boldsymbol{\tau}^{(1)} = U v_x^\varepsilon + U \varepsilon \left(\partial_x w v_z^\varepsilon - \varepsilon \frac{v_x^\varepsilon}{2} (\partial_x w)^2 \right) + O(\varepsilon^3)$$

and an analogous expression for $\mathbf{v} \cdot \boldsymbol{\tau}^{(2)}$.

3.1.4. A kinematic condition for the fracture boundary. For later purposes, we recall the kinematic boundary condition for the fracture boundary (cf. [68]). In the normal direction we impose

$$(3.14) \quad \frac{Dh}{Dt} - v_{out} = \partial_t h - v_{out} + (v_1, v_2) \cdot \nabla_{x_1, x_2} h - v_3 = 0 \quad \text{on } x_3 = h(x_1, x_2, t).$$

The term v_{out} ensures mass conservation inside the fracture and is well known as the leak-off q_L . In the dimensionless form, the condition reads

$$(3.15) \quad \partial_t w + (v_x^\varepsilon, v_y^\varepsilon) \cdot \nabla_{x,y} w - v_z^\varepsilon = -v_{LO} \quad \text{on } z = w(x, y, t),$$

$$\text{where } v_{LO} = \frac{v_{out}}{U\varepsilon}.$$

3.1.5. A second rescaled system by using the lubrication assumptions. As in lubrication theory, we can now expand the velocities, pressure, and viscosities as follows:

$$(3.16) \quad v_x^\varepsilon = v_x^0 + \varepsilon^2 v_x^1 + O(\varepsilon^4), \quad v_y^\varepsilon = v_y^0 + \varepsilon^2 v_y^1 + O(\varepsilon^4), \quad v_z^\varepsilon = v_z^0 + \varepsilon^2 v_z^1 + O(\varepsilon^4),$$

$$(3.17) \quad p^\varepsilon = p^0 + \varepsilon^2 p^1 + O(\varepsilon^4),$$

$$(3.18) \quad \eta^\varepsilon = \eta^0 + \varepsilon^2 \eta^1 + O(\varepsilon^4).$$

Here, the upper indices 0 and 1 denote the respective order of the underlying expansions. We recall that the fracture boundary given by (3.1) is given in dimensionless form by

$$(3.19) \quad \begin{cases} +w(x, y, t) & \text{for } z \geq 0, \\ -w(x, y, t) & \text{for } z < 0. \end{cases}$$

Inserting (3.16)–(3.19) into (3.7)–(3.11) yields, on the order $O(1)$ in Ω_F ,

$$(3.20) \quad -\partial_x p^0 + \partial_z (\eta^0 \partial_z v_x^0) = 0, \quad -\partial_y p^0 + \partial_z (\eta^0 \partial_z v_y^0) = 0, \quad -\partial_z p^0 = 0,$$

$$(3.21) \quad \partial_x v_x^0 + \partial_y v_y^0 + \partial_z v_z^0 = \bar{q},$$

$$(3.22) \quad \partial_t \eta^0 + \partial_x (\eta^0 v_x^0) + \partial_y (\eta^0 v_y^0) + \partial_z (\eta^0 v_z^0) = \bar{q} \eta^0.$$

Specifically, on the fracture boundary w , we have

$$(3.23) \quad v_x^0(x, y, w, t) = v_y^0(x, y, w, t) = 0,$$

which can be seen with the help of (3.13) using the leading order term.

3.1.6. Derivation of a pressure lubrication equation. Following [90], we use (3.20)–(3.23) to calculate v_x^0, v_y^0 and obtain a PDE for p^0 . We first compute the permeability, which depends nonlocally on the viscosity η :

(3.24)

$$K(\eta^0, x, y, z, t) = \int_{-w}^z \frac{\xi + w}{\eta^0(t, x, y, \xi)} d\xi - \int_{-w}^w \frac{\xi + w}{\eta^0(t, x, y, \xi)} d\xi \frac{\int_{-w}^z \frac{1}{\eta^0(t, x, y, \xi)} d\xi}{\int_{-w}^w \frac{1}{\eta^0(t, x, y, \xi)} d\xi},$$

$$(3.25) \quad v_x^0 = K \partial_x p^0, \quad v_y^0 = K \partial_y p^0, \quad \partial_t w = v_z^0(x, y, w) - v_{LO}.$$

Next we average the continuity equation (3.21) with respect to z , which yields

$$(3.26) \quad \partial_x \int_{-w}^w v_x^0 dz + \partial_y \int_{-w}^w v_y^0 dz + v_z^0(x, y, w(x, y, t), t) - v_z^0(x, y, -w(x, y, t), t) = \int_{-w}^w \bar{q} dz.$$

Employing the kinematic condition (3.15) with (3.23) yields

$$v_z^0(x, y, w(x, y, t), t) = \partial_t w + v_{LO}.$$

Then, (3.26) yields

$$(3.27) \quad \partial_x \int_{-w}^w v_x^0 dz + \partial_y \int_{-w}^w v_y^0 dz + 2\partial_t w - [v_{LO}]_{-w}^w = \int_{-w}^w \bar{q} dz.$$

Equation (3.27) is the Reynolds lubrication equation (see [90]). It is usually written in terms of the pressure and we introduce K^{abs} (which has no relationship with the absolute permeability) such that

$$\int_{-w}^w v_x^0 \, dz = -K^{abs}(x, y, t) \partial_x p^0 \quad \text{and} \quad \int_{-w}^w v_y^0 \, dz = -K^{abs}(x, y, t) \partial_y p^0.$$

Using (3.24) and (3.25) yields

$$(3.28) \quad -K^{abs}(x, y, t) = \int_{-w}^w \frac{(\xi + w)(w - \xi)}{\eta^0(t, x, y, \xi)} \, d\xi - \int_{-w}^w \frac{\xi + w}{\eta^0(t, x, y, \xi)} \, d\xi \frac{\int_{-w}^w \frac{w - \xi}{\eta^0(t, x, y, \xi)} \, d\xi}{\int_{-w}^w \frac{1}{\eta^0(t, x, y, \xi)} \, d\xi}.$$

In (3.28) K^{abs} depends on η^0 nonlocally and (3.27), and is written in the form of Reynolds' equation

$$(3.29) \quad 2\partial_t w - \partial_x(K^{abs} \partial_x p^0) - \partial_y(K^{abs} \partial_y p^0) = \int_{-w}^w \bar{q} \, dz + [v_{LO}]_{-w}^w.$$

3.1.7. Derivation of a PDE lubrication system for pressure and saturation. So far, the derivation in the previous section 3.1.6 has been performed without any additional assumptions on the two fluids. We now focus our attention on a specific case when η^0 can be downscaled. More precisely (see [64]), we assume

$$(3.30) \quad \eta^\varepsilon = M \chi_{\{-a(x_1, x_2) \leq z \leq a(x_1, x_2)\}} + \chi_{\{-w \leq z < -a(x_1, x_2) \text{ and } a(x_1, x_2) < z \leq w\}},$$

which means that the injecting fluid with viscosity $\eta_{F,\text{inj}}$ does not touch the fracture boundary w . Moreover, we note that it is compatible with the initial condition (3.12). The integrals involving η^0 can be evaluated as a function of the unknown free boundary a yielding

$$(3.31) \quad K^{abs} = \frac{2}{3} \left(\frac{a^3}{M} + w^3 - a^3 \right).$$

Remark 3.2. Permeability laws for single phase fluids have been derived in [68] for Newtonian and in [52] for non-Newtonian flows. For instance, $M = 1$ yields

$$(3.32) \quad K^{abs} = \frac{2w^3}{3}.$$

At this stage, it is convenient to introduce the saturation

$$(3.33) \quad s = \frac{a}{w},$$

and (3.31) becomes

$$(3.34) \quad K^{abs} = \frac{2w^3}{3} \left(\frac{s^3}{M} + 1 - s^3 \right).$$

We denote that $s_{F,\text{res}}$ is the saturation for the residing fluid and $s_{F,\text{inj}}$ is the saturation for the injection fluid into the fracture. Also, $p_{F,\text{res}}$ is the pressure for residing fluid and $p_{F,\text{inj}}$ is the pressure for injection fluid in a fracture. For simplicity, in this section, we abuse the notation by defining

$$s := s_{F,\text{inj}}, \quad 1 - s := s_{F,\text{res}},$$

and

$$p^0 := (p^0)_{F,\text{inj}}.$$

We recall that the 0 in the superscript denotes the order of our previous expansions. Here, we only work with the leading order 0 and neglect all further orders 1, 2, 3, Moreover, recall that

$$(3.35) \quad s_{F,\text{res}} + s_{F,\text{inj}} = 1$$

and

$$(3.36) \quad p_c := p_{F,\text{res}} - p_{F,\text{inj}},$$

where p_c is a capillary pressure which will be discussed in detail in section 3.1.8.

We still miss one equation and we use the nonmiscibility condition (3.2) and its zero order expansion approximation (3.22) to get

$$(3.37) \quad \partial_t a + v_x^0(x, y, a, t) \partial_x a + v_y^0(x, y, a, t) \partial_y a - v_z(x, y, a, t) = 0.$$

Integrating (3.21), from a to w with respect to z , yields

$$(3.38) \quad \begin{aligned} -v_z(x, y, a, t) &= \int_a^w \bar{q} \, dz - v_x^0(x, y, a, t) \partial_x a - v_y^0(x, y, a, t) \partial_y a \\ &\quad - \partial_x \int_a^w v_x^0 \, dz - \partial_y \int_a^w v_y^0 \, dz - v_{LO} - \partial_t w. \end{aligned}$$

After plugging (3.38) into (3.37) we obtain

$$(3.39) \quad \partial_t a - \partial_x \int_a^w v_x^0 \, dz - \partial_y \int_a^w v_y^0 \, dz = v_{LO} + \partial_t w.$$

A direct calculation gives

$$(3.40) \quad \int_a^w v_x^0 \, dz = -\frac{w^3}{6}(1-s)^2(2+s)\partial_x p^0 = \left(\int_a^w K \, dz\right) \partial_x p^0.$$

Inserting (3.40) into (3.39) yields

$$(3.41) \quad \partial_t(w(s-1)) + \nabla_{x,y} \cdot \left(\frac{w^3}{6}(1-s)^2(2+s)\nabla_{x,y} p^0 \right) = v_{LO}.$$

Remark 3.3. We note that (3.41) is not valid in the fracture tip region and that the two fluid Stokes equations (3.3)–(3.6) do not simplify there. Computationally, however we do not solve the Stokes equations, but work with a cake region [46] and appropriate interpolations that are motivated and explained in [68](Remark 2.2) and [56](Remark 3).

Our results can be summarized as follows: The lubrication approximation for the velocity and the pressure solutions to two phase Stokes system (3.3)–(3.6), (3.13)–(3.13), with the compatibility hypothesis (3.12), reads as follows.

FORMULATION 2. *For s and $1-s$, we solve, respectively,*

$$(3.42) \quad \partial_t(w(1-s)) - \nabla_{x,y} \cdot \left(\frac{w^3}{3} \frac{(1-s)^2}{2}(2+s)\nabla_{x,y} p^0 \right) = -v_{LO} + \int_a^w \bar{q} \quad \text{in } \omega \times (0, T),$$

$$(3.43) \quad \partial_t(ws) - \nabla_{x,y} \cdot \left(\frac{w^3}{3M} \left(s^3 + \frac{3s}{2}(1-s^2)M \right) \nabla_{x,y} p^0 \right) = \int_0^a \bar{q} \quad \text{in } \omega \times (0, T)$$

and for the leading order of the pressure p^0 , we solve

$$(3.44) \quad \partial_t w - \nabla_{x,y} \cdot \left(\frac{w^3}{3} \left(1 - s^3 + \frac{s^3}{M} \right) \nabla_{x,y} p^0 \right) = \int_0^w \bar{q} \, dz - v_{LO} \quad \text{in } \omega \times (0, T).$$

The initial conditions for the interface between the two fluids, the fracture width, and saturation are given by

$$(3.45) \quad a|_{t=0} = a_0,$$

$$(3.46) \quad w|_{t=0} = w_0,$$

$$(3.47) \quad s|_{t=0} = a_0/w_0 \quad \text{in } \omega.$$

The relative permeabilities are given by

$$(3.48) \quad k_{F,res}(s) := \frac{1}{2}(1-s)^2(2+s), \quad k_{F,inj}(s) := s^3 + \frac{3s(1-s^2)}{2}M,$$

and the fractional flow curve is

$$(3.49) \quad F(s) := \frac{s^3 + \frac{3s(1-s^2)}{2}M}{s^3 + (1-s^3)M}.$$

Remark 3.4. We remark that the relative permeabilities are equivalent to the laws stated in [35], which were compared to the experimental data from [34]. The agreement was not very good and justified by an inaccuracy of the experimental data. On the other, the agreement was good when the saturation variable was replaced by the Lockhart–Martinelli factor $\chi_{LM} = \frac{k_{F,res}}{k_{F,inj}}$. Dropping the surface pressure between fluids could also be a source of inaccuracy and our solution consists in adding the capillary pressure introduced in [10] to the model.

Remark 3.5. Under assumptions that the BV-norm of η^ε is uniformly bounded with respect to ε , a justification of the upscaled model was obtained by Paoli in [79].

3.1.8. The capillary pressure function for a penny-shaped fracture. In the previous section, we have assumed that the capillary pressure is zero. Knowledge of the relative permeabilities is crucial for the numerical simulation of the multiphase flows through porous media. Nevertheless, the models where the dissipation is absent lead to the Buckley–Leverett equation, which is a hyperbolic conservation law. The solutions lose regularity in finite time and discontinuous solutions are not unique. In order to have uniqueness, the Oleinik entropy criterion (or, equivalently, the Welge method [93] in petroleum engineering) is employed; see [25]. Nevertheless, recent questions about entropies associated with two phase flow and the application of Oleinik entropy has arisen. For more details we refer to the analytical work by van Duijn, Peletier and Pop [92] justifying experimental observations by DiCarlo in [29].

A natural remedy is to add the physical dissipation linked to the surface tension. Classically it is taken into account through the capillary pressure. A more recent approach is to use a Cahn–Hilliard-type phase-field equations, as in [26], which involves a fourth order differential operator in the flow equations. This is nonstandard for the complex flows simulations with industrial applications. We choose to calculate the capillary pressure function from our relative permeabilities, using the interface energy approach from [10].

Following the approach from [10], we use, as capillary pressure,

$$(3.50) \quad p_c(s) = \gamma_{res} \cos \theta \sqrt{\frac{\phi}{K_c}} ((k_{F,res}(s))^{-1/2} + (k_{F,inj}(s))^{-1/2})(1-s) + C,$$

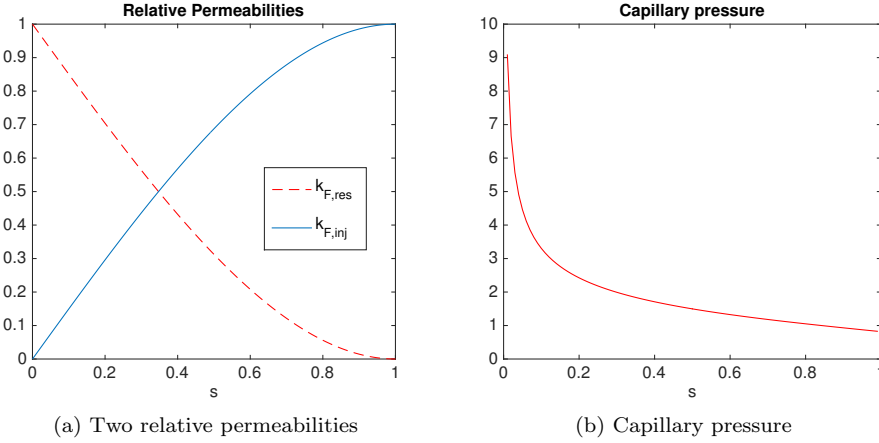


FIG. 2. Two relative permeabilities (3.48) and a capillary pressure are illustrated for the case $M = 1$.

where γ_{res} is the phase surface energy between two different phases, θ is the injecting-phase contact angle, and $K_c = \frac{2H^2w^2}{3}$. The constant C corresponds to initial displacement pressure. For imbibition, we set $C = 0$ and $k_{F,\text{res}}$ and $k_{F,\text{inj}}$ are given by (3.48). See Figure 2.

3.1.9. The final two dimensional (2D) lubrication system: An upscaled two phase model for fracture flow. After including the capillary pressure, our upscaled dimensional model for the two phase flow in the fracture Ω_F reads as follows.

FORMULATION 3. Find the saturations $1 - s$ and s such that

$$(3.51) \quad \partial_t(h(1-s)) - \nabla_{x,y} \cdot \left(\frac{h^3}{3\eta_{F,\text{res}}} k_{F,\text{res}} \nabla_{x,y} p_{F,\text{res}} \right) = -v_{\text{out}} + \int_{sh}^h q \, dx_3 \quad \text{in } \omega \times (0, T),$$

$$(3.52) \quad \partial_t(hs) - \nabla_{x,y} \cdot \left(\frac{h^3}{3\eta_{F,\text{inj}}} k_{F,\text{inj}} \nabla_{x,y} p_{F,\text{inj}} \right) = \int_0^{sh} q \, dx_3 \quad \text{in } \omega \times (0, T),$$

and find the pressure $p_{F,\text{inj}}$ such that

$$(3.53) \quad \begin{aligned} \partial_t h - \nabla_{x,y} \cdot \left(\frac{h^3}{3} \left(\frac{k_{F,\text{res}}}{\eta_{F,\text{res}}} + \frac{k_{F,\text{inj}}}{\eta_{F,\text{inj}}} \right) \nabla_{x,y} p_{F,\text{inj}} + \frac{h^3}{3} \frac{k_{F,\text{res}}}{\eta_{F,\text{res}}} \nabla_{x,y} p_c(s) \right) \\ = \frac{1}{2} \int_{-h}^h q \, dx_3 - v_{\text{out}} \quad \text{in } \omega \times (0, T), \end{aligned}$$

or find the pressure $p_{F,\text{res}}$ such that

$$(3.54) \quad \begin{aligned} \partial_t h - \nabla_{x,y} \cdot \left(\frac{h^3}{3} \left(\frac{k_{F,\text{res}}}{\eta_{F,\text{res}}} + \frac{k_{F,\text{inj}}}{\eta_{F,\text{inj}}} \right) \nabla_{x,y} p_{F,\text{res}} - \frac{h^3}{3} \frac{k_{F,\text{inj}}}{\eta_{F,\text{inj}}} \nabla_{x,y} p_c(s) \right) \\ = \frac{1}{2} \int_{-h}^h q \, dx_3 + \frac{1}{2} [v_{LO}]_w^w \quad \text{in } \omega \times (0, T), \end{aligned}$$

where

$$\frac{k_{F,\text{res}}}{\eta_{F,\text{res}}} + \frac{k_{F,\text{inj}}}{\eta_{F,\text{inj}}} = \left(\frac{s^3}{\eta_{F,\text{inj}}} + \frac{1-s^3}{\eta_{F,\text{res}}} \right)$$

with the initial conditions

$$(3.55) \quad s|_{t=0} = s_0 = A_0/h_0,$$

$$(3.56) \quad h|_{t=0} = h_0.$$

Here the phase velocities are

$$(3.57) \quad \frac{1}{2h} \left(\int_{-h}^{-sh} + \int_{sh}^h \right) (v_x^0, v_y^0) = \frac{1}{h} \int_{sh}^h (v_x^{\text{res}}, v_y^{\text{res}}) dx_3 = -\frac{K_F}{\eta_{F,\text{res}}} k_{F,\text{res}}(s) \nabla_{x,y} p_{F,\text{res}},$$

$$(3.58) \quad \frac{1}{2h} \left(\int_{-h}^{-sh} + \int_{sh}^h \right) (v_x^0, v_y^0) = \frac{1}{h} \int_0^{sh} (v_x^{\text{inj}}, v_y^{\text{inj}}) dx_3 = -\frac{K_F}{\eta_{F,\text{inj}}} k_{F,\text{inj}}(s) \nabla_{x,y} p_{F,\text{inj}}$$

with the absolute permeability

$$K_F = \frac{h^2}{3}.$$

Remark 3.6. Due to the relations (3.35) and (3.36), it is sufficient to solve only one of the saturation equations (3.51)–(3.52) and analogously only the pressure equation (3.53). To concentrate on one of the respective equations is done in section 3.1.10.

3.1.10. A 3D two phase flow system. We now use (3.51)–(3.53) and substitute them into a classical 3D two phase flow model in a fracture. The background of this procedure is similar to the ideas presented in [52] and [68] for single phase flow and quasi-Newtonian flow, respectively. In our global systems, we recall that we have two variables for the saturation in a fracture denoted by $s_{F,\text{inj}}$ (the saturation for the residing fluid) and $s_{F,\text{res}}$ (saturation for the injection fluid), and three variables for the pressure denoted by $p_R, p_{F,\text{inj}}, p_{F,\text{res}}$, where p_R is the pressure for the reservoir, $p_{F,\text{res}}$ is the pressure for residing fluid in a fracture, and $p_{F,\text{inj}}$ is the pressure for the injection fluid in a fracture. However after employing the relation

$$(3.59) \quad s_{F,\text{inj}} + s_{F,\text{res}} = 1 \quad \text{and} \quad p_c = p_{F,\text{res}} - p_{F,\text{inj}},$$

where p_c is referred as the capillary pressure in a fracture, we only solve for the saturation and the pressure of the injecting fluid, $s_{F,\text{inj}}, p_{F,\text{inj}}$, in a fracture as described in Remark 3.6.

In the reservoir, we have p_R , but a saturation variable is not defined since we assume a single phase fluid in the reservoir; see Figure 3 for more details. Thus, we obtain the following Formulation 4 from Formulation 3 by rewriting (3.52) and (3.53).

FORMULATION 4. Find $s_{F,\text{inj}}$ such that

$$(3.60a) \quad \partial_t (\phi_F^* s_{F,\text{inj}}) - \nabla \cdot \left(K_F \frac{k_{F,\text{inj}}(s_{F,\text{inj}})}{\eta_{F,\text{inj}}} \nabla p_{F,\text{inj}} \right) = q_{F,\text{inj}} \quad \text{in } \Omega_F \times (0, T),$$

$$(3.60b) \quad K_F \frac{k_{F,\text{inj}}(s_{F,\text{inj}})}{\eta_{F,\text{inj}}} \nabla p_{F,\text{inj}} \cdot \mathbf{n}_F = 0 \quad \text{on } \Gamma_F(t) \times (0, T),$$

where ϕ_F^* is the porosity of the fracture which is set to one, and $\eta_{F,\text{res}}, \eta_{F,\text{inj}}$ are the viscosities for each fluid, respectively. Moreover, $q_{F,\text{inj}} := \tilde{s}_{F,\text{inj}} \tilde{q}_{F,\text{inj}}$, where $\tilde{s}_{F,\text{inj}}, \tilde{q}_{F,\text{inj}}$ are the saturation injection/production terms and flow injection/production, respectively. If $\tilde{q}_{F,\text{inj}} > 0$, $\tilde{s}_{q,\text{inj}}$ is the injected saturation of the fluid and if $\tilde{q}_{F,\text{inj}} < 0$, $\tilde{s}_{q,\text{inj}}$ is the produced saturation. We note that $\tilde{s}_{q,\text{inj}} + \tilde{s}_{q,\text{res}} = 1$.

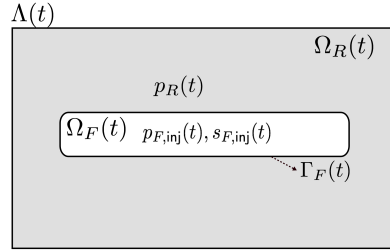


FIG. 3. Illustration of different domains and variables. The middle void area is a fracture zone, $\Omega_F(t)$. Here, $p_R(t)$ is the pressure value in the reservoir domain $\Omega_R(t)$ and $s_{F,inj}$ and $p_{F,inj}$ are injecting fluid saturation and pressure in a fracture, respectively.

In addition, find the pressure $p_{F,inj}$ such that

$$(3.61) \quad -\nabla \cdot (K_F \lambda_{tot} \nabla p_{F,inj} + K_F \lambda_{F,res} \nabla p_c(s_{F,inj})) = (q_F)_{tot} \quad \text{in } \Omega_F(t) \times (0, T),$$

Here the total mobility, the mobility for the injecting fluid, and the mobility for the residing fluid, are defined, respectively,

$$(3.62a) \quad \lambda_{tot} := \lambda_{tot}(s_{F,inj}) = \lambda_{F,inj}(s_{F,inj}) + \lambda_{F,res}(s_{F,inj}),$$

$$(3.62b) \quad \lambda_{F,inj} := \lambda_{F,inj}(s_{F,inj}) = \frac{k_{F,inj}(s_{F,inj})}{\eta_{F,inj}},$$

$$(3.62c) \quad \lambda_{F,res} := \lambda_{F,res}(s_{F,inj}) = \frac{k_{F,res}(s_{F,inj})}{\eta_{F,res}},$$

$$(3.62d) \quad \text{and } (q_F)_{tot} := q_{F,inj} + q_{F,res}.$$

The above formulation is similar to the two phase flow model in porous media as discussed in [8, 24, 32, 43, 49], but we have computed new relative permeabilities (3.48) and employ a capillary pressure (3.50) to consider two phase flow in a fracture.

Remark 3.7. Similar to the literature [99, 101], the original lubrication law has a cubic power in which the width parameter h in the time derivative replaces the porosity. By dividing the flux over the cross-sectional area (see, for example, page 5 in [101]), we “lose” one order and arrive at a quadratic law.

4. Single-phase flow in the reservoir. We briefly recapitulate the standard single phase flow model that we employ in the porous medium. Continuity of mass is modeled as

$$(4.1) \quad \partial_t(\rho_R \phi_R^*) + \nabla \cdot (\rho_R \mathbf{v}_R) = \rho_R q_R \quad \text{in } \Omega_R \times (0, T).$$

Here ρ_R is the fluid density in reservoir and q_R is a source/sink term. We assume the fluid in the reservoir is slightly compressible, thus we define the fluid density as

$$(4.2) \quad \rho_R := \rho_R^0 \exp(c_R(p_R - p_R^0)) \approx \rho_R^0(1 + c_R(p_R - p_R^0)),$$

where $p_R : \Omega_R \times [0, T] \rightarrow \mathbb{R}$ is the pressure, p_0 is the initial pressure at $t = 0$, ρ_R^0 is the reference density, and c_R is the fluid compressibility. In addition, ϕ_R^* is the reservoir fluid fraction and

$$(4.3) \quad \phi_R^* := \phi_0^* + \alpha \nabla \cdot \mathbf{u} + \frac{1}{M_B}(p_R - p_0).$$

Here $\mathbf{u} : \Omega \times [0, T] \rightarrow \mathbb{R}^d$ is the solid displacement, $\alpha \in [0, 1]$ is the Biot coefficient, $M_B > 0$ is a given Biot modulus, and ϕ_0^* is the initial fluid fraction value. Next, we describe the flow given by Darcy's law,

$$(4.4) \quad \mathbf{v}_R = -\frac{K_R}{\eta_R} \nabla p_R,$$

where η_R is the fluid viscosity, K_R is the permeability for the reservoir.

Following the general reservoir approximation with the assumption that c_R is small enough, we use $\rho_R = \rho_R^0$ and assume $p_0 = 0$, to rewrite (4.1) as

$$(4.5) \quad \partial_t \left(\frac{1}{M_B} p_R + \alpha \nabla \cdot \mathbf{u} \right) - \nabla \cdot \frac{K_R}{\eta_R} \nabla p_R = q_R \quad \text{in } \Omega_R \times (0, T).$$

The system is supplemented with initial and boundary conditions. The initial conditions are given by

$$p_R(\mathbf{x}, 0) = p_R^0 \quad \text{for all } \mathbf{x} \in \Omega_R(t=0),$$

where p_R^0 is a smooth given pressure. To determine the initial location of Γ_F at $t = 0$, we also have

$$\phi(\mathbf{x}, 0) = \phi^0 \quad \text{for all } \mathbf{x} \in \Lambda(t=0),$$

where ϕ^0 is a given smooth initial fracture. We finally prescribe the boundary and interface conditions for pressure as

$$(4.6a) \quad K_R \nabla p_R \cdot \mathbf{n} = 0 \quad \text{on } \partial \Lambda \times (0, T),$$

$$(4.6b) \quad p_R = p_{F,\text{res}} \quad \text{on } \Gamma_F \times (0, T),$$

$$(4.6c) \quad \frac{K_R}{\eta_R} \nabla p_R \cdot \mathbf{n}_F = \frac{K_F k_{F,\text{res}}}{\eta_{F,\text{res}}} \nabla p_{F,\text{res}} \cdot \mathbf{n}_F \quad \text{on } \Gamma_F \times (0, T),$$

where $\rho_{F,\text{res}}$ is the residing fluid density in fracture.

5. Coupling algorithms, variational formulations, and discretization.

This section presents frameworks for the numerical solution of the previously introduced equations. We introduce the following equation settings: a displacement/phase-field framework, a crack-width problem, a pressure diffraction problem, and a saturation formulation. For coupling flow (pressure and saturation) and geomechanics (displacement/phase-field), we employ iterative fixed-stress coupling. Moreover, for consistent modeling of the flow equations, we introduce diffraction systems for which we explain the decomposition of the domain $\Lambda(t)$ into appropriate time-dependent subdomains.

5.1. Preliminaries. For the spatial discretization, we utilize Galerkin finite element methods. In particular, we employ continuous Galerkin (CG) finite elements for displacements and phase-field, and an enriched Galerkin (EG) finite elements for both the pressure and saturation equations in order to obtain local mass conservation with an efficient solver. In porous media flow it is well known that the velocities should be locally mass conservative to avoid unphysical spurious oscillations. This can either be achieved by postprocessing of the velocities [89] or by a direct solution from the appropriate function space. We employ the latter method, the EG, that was first proposed in [88] for elliptic problems and was extended to parabolic and hyperbolic cases in [49–51] with efficient solvers and dynamic mesh adaptivity.

We consider a shape regular mesh family and we assume that each mesh \mathcal{T} is a subdivision of $\bar{\Lambda}$ made of disjoint elements \mathcal{K} , i.e., squares when $d = 2$ or cubes when $d = 3$. Each subdivision is assumed to exactly approximate the computational domain, thus $\bar{\Lambda} = \cup_{K \in \mathcal{T}} K$. The diameter of an element $K \in \mathcal{T}$ is denoted by h_K and we denote h_{\min} and h_{\max} for the minimum and maximum diameters, respectively.

The EG method requires (similar to discontinuous Galerkin) additional notations due to face term contributions. We let \mathcal{E}_h be the set of all edges/faces and \mathcal{E}_h^o and \mathcal{E}_h^∂ are the collection of all interior and boundary edges/faces, respectively. In the following, we use the notation for edges in two dimension but the results hold analogously for faces in three dimensions. The boundary edges \mathcal{E}_h^∂ can be further decomposed into $\mathcal{E}_h^\partial = \mathcal{E}_h^{D,\partial} \cup \mathcal{E}_h^{N,\partial}$, where $\mathcal{E}_h^{D,\partial}$ is the collection of edges where Dirichlet boundary conditions are imposed, while $\mathcal{E}_h^{N,\partial}$ is the collection of edges where Neumann boundary conditions are imposed. In addition, we denote that $\mathcal{E}_h^1 := \mathcal{E}_h^o \cup \mathcal{E}_h^{D,\partial}$. For any $e \in \mathcal{E}_h^o$, let \mathcal{K}_+ and \mathcal{K}_- be two neighboring elements such that $e = \partial\mathcal{K}_+ \cap \partial\mathcal{K}_-$. We denote by h_e the maximum length of the edges e . Let \mathbf{n}_+ and \mathbf{n}_- be the outward normal unit vectors to $\partial\mathcal{K}_+$ and $\partial\mathcal{K}_-$, respectively ($\mathbf{n}_\pm := \mathbf{n}|_{\mathcal{K}_\pm}$). For any given function, vector, or matrix ξ defined on the triangulation \mathcal{T} , we denote ξ_\pm by the restrictions of ξ to \mathcal{K}_\pm . The space $H^k(\mathcal{T})$ ($k \in \mathbb{N}$) is the set of elementwise H^k functions on \mathcal{T} , and $L^2(\mathcal{E}_h)$ refers to the set of functions whose traces on the elements of \mathcal{E}_h are square integrable. In addition, we define the average $\{\!\{ \cdot \}\!\}$ as follows:

$$(5.1) \quad \{\!\{ w \}\!\} := \frac{1}{2}(w_+ + w_-) \text{ for } w \in [L^2(\mathcal{T})]^d,$$

$$(5.2) \quad \{\!\{ w \}\!\} := \frac{1}{2}(w_+ + w_-) \text{ for } w \in [L^2(\mathcal{T})]^{d \times d},$$

$$(5.3) \quad \text{and } \{\!\{ w \}\!\} := w \text{ for } e \in \mathcal{E}_h^\partial.$$

The jump across the interior edge will be defined as

$$[w] = w_+ \mathbf{n}_+ + w_- \mathbf{n}_- \text{ on } e \in \mathcal{E}_h^o \quad \text{and} \quad [w] = w \mathbf{n} \text{ for } e \in \mathcal{E}_h^\partial.$$

For any integer $k \geq 1$ and any $\mathcal{K} \in \mathcal{T}$, we denote by $\mathbb{Q}^k(\mathcal{K})$ the space of scalar-valued multivariate polynomials over \mathcal{K} of partial degree at most k . The vector-valued counterpart of $\mathbb{Q}^k(\mathcal{K})$ is denoted $\mathbb{Q}^k(\mathcal{K})$.

Temporal discretization is performed with an A-stable backward Euler finite difference scheme. Here, we define a partition of the time interval $0 =: t^0 < t^1 < \dots < t^N := T$ and denote the time step size by $\delta t := t^n - t^{n-1}$.

5.2. Global algorithms and fixed stress iterative coupling. To facilitate the understanding of the overall numerical solution, we first present in this section the global coupling algorithm based on a fixed-stress iteration. The fixed-stress coupling scheme is well known in subsurface modeling, environmental, and petroleum engineering problems [22, 44, 45, 65, 66, 84, 85]. The idea is to iterate between flow and geomechanics at each time step until sufficient accuracy is achieved. For detailed explanations and numerical demonstrations using phase-field fracture, we refer to [56]. The algorithm used in this paper is provided in Figure 4. A theoretical justification of the fixed-stress phase-field fracture scheme in which the phase-field values are assumed to be given has been recently shown in [3]. Computational evidence from several numerical tests, including a fluid filled Sneddon test [87] has been gathered in [56].

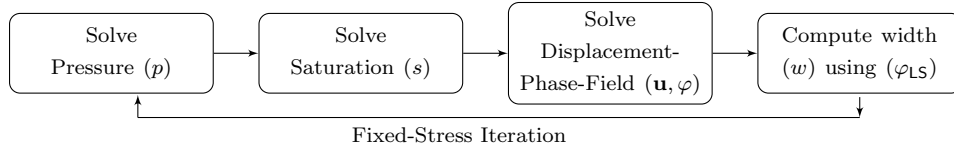


FIG. 4. The global algorithm flowchart. During the fixed-stress iteration, an iterative implicit pressure explicit saturation formulation is embedded.

5.2.1. Notations for spatial, temporal, and fixed-stress discretizations.

For the following, we introduce the necessary notation. We denote by l the fixed-stress iteration index and by n the time step index. Thus, the spatial approximations of the functions

$$\mathbf{u}(\mathbf{x}, t), \varphi(\mathbf{x}, t), \varphi_{\text{LS}}(\mathbf{x}, t), w(\mathbf{x}, t), p(\mathbf{x}, t), s(\mathbf{x}, t)$$

are denoted by

$$\mathbf{U}, \Phi, \Phi_{\text{LS}}, W, P, S.$$

The functions $\varphi_{\text{LS}}(\mathbf{x}, t)$, $w(\mathbf{x}, t)$, and Φ_{LS} , W , respectively, have not been introduced yet. They stand for a level set function and a width approximation problem introduced in [56]. Details of the numerical solution are provided below in section 5.4.

The approximation of each function in time $0 \leq n \leq N$ is denoted by

$$\mathbf{U}^n, \Phi^n, \Phi_{\text{LS}}^n, W^n, P^n, S^n,$$

where $\mathbf{U}^n := \mathbf{U}(t^n)$ at time t^n and so forth. At each time step n , we have an inner loop indexed by $l = 1, 2, 3, \dots$ and we denote the fixed stress iterative solutions for each time step by

$$\mathbf{U}^l := \mathbf{U}^{n,l}, \Phi^l := \Phi^{n,l}, \Phi_{\text{LS}}^l := \Phi_{\text{LS}}^{n,l}, W^l := W^{n,l}, P^l := P^{n,l}, S^l := S^{n,l}.$$

Moreover, we set as an initial fixed-stress step $\mathbf{U}^{n,0} := \mathbf{U}^{n-1}$ and so forth.

5.2.2. The final algorithm. The overall solution loop is presented in Algorithm 1.

5.3. Displacements and phase-field. Based on Formulation 1, we derive a variational incremental formulation. Therein, the continuous irreversibility constraint $\partial_t \varphi \leq 0$ is approximated by $\varphi \leq \varphi^{old}$.

The discrete solution variables are denoted by \mathbf{U} and Φ (approximating \mathbf{u} and ϕ), respectively. In more detail, we have $\mathbf{U} \in \mathcal{C}^0([0, T]; \mathbf{V}(\mathcal{T}))$ and $\Phi \in \mathcal{C}^0([0, T]; \mathbb{Z}(\mathcal{T}))$, where

$$(5.4) \quad \mathbf{V}(\mathcal{T}) := \{V \in C^0(\bar{\Lambda}; \mathbb{R}^d) \mid V = \mathbf{0} \text{ on } \partial\Lambda, V|_{\mathcal{K}} \in \mathbb{Q}^1(\mathcal{K}), \forall \mathcal{K} \in \mathcal{T}\},$$

$$(5.5) \quad \mathbb{Z}(\mathcal{T}) := \{Z \in C^0(\bar{\Lambda}; \mathbb{R}) \mid Z^n \leq Z^{n-1} \leq 1, Z|_{\mathcal{K}} \in \mathbb{Q}^1(\mathcal{K}), \forall \mathcal{K} \in \mathcal{T}\}.$$

Moreover, we extrapolate Φ (denoted by $E(\Phi)$) in some terms in order to avoid an indefinite Hessian matrix [41]. That is to say, we take the two previous time step solutions at t^{n-1} and t^{n-2} and evaluate at time t :

$$E(\Phi^{n,l}) = \Phi^{n-2} + \frac{(t - t^{n-1} - t^{n-2})}{(t - t^{n-1}) - (t - t^{n-1} - t^{n-2})} (\Phi^{n-1} - \Phi^{n-2}).$$

For the solution process, we define a semi linear form in the following.

Algorithm 1. Iterative coupling for two phase flow phase-field fractures including level set and width computations.

Initial conditions : Let $\Phi^{n-1}, \mathbf{U}^{n-1}, P^{n-1}, S^{n-1}, \Phi_{LS}^{n-1}, W^{n-1}$ be given.

At time t^n :

repeat

For $l = 1, 2, 3, \dots$:

- Solve the pressure diffraction Formulation 7 for the reservoir pressure and for the injecting phase $P^l = P_{F,\text{inj}}^l$
- Solve the saturation diffraction Formulation 8 for the injecting phase $S^l = S_{F,\text{inj}}^l$
- Solve the quasi-monolithic displacement/phase-field Formulation 5 for (\mathbf{U}^l, Φ^l)

- Compute the level set Φ_{LS}^l and solve the width Formulation 6 for W^l

until the stopping criterion for fixed-stress split is satisfied:

$$\max\{\|P^l - P^{l-1}\|, \|\mathbf{U}^l - \mathbf{U}^{l-1}\|, \|\Phi^l - \Phi^{l-1}\|\} \leq \text{TOL}_{FS}, \quad \text{TOL}_{FS} > 0$$

Set: $(P^n, \mathbf{U}^n, \Phi^n, S^n) := (P^l, \mathbf{U}^l, \Phi^l, S^l)$.

The other two variables Φ_{LS}^n and W^n are obtained from Φ^n and \mathbf{U}^n .

Increment the time $n \rightarrow n + 1$.

FORMULATION 5. Let us assume that $P^l := P^{n,l}$ is a given pressure at the time t^n and at the fixed-stress iteration l . Given the initial conditions \mathbf{U}^{l-1} and Φ^{l-1} we seek $\{\mathbf{U}^l, \Phi^l\} \in \mathbf{V}(\mathcal{T}) \times \mathbb{Z}(\mathcal{T})$ such that

$$(5.6) \quad \mathcal{A}(\mathbf{U}^l, \Phi^l)(\mathbf{w}, \psi - \Phi^l) \geq 0 \quad \forall \{\mathbf{w}, \psi\} \in \mathbf{V}(\mathcal{T}) \times \mathbb{Z}(\mathcal{T}),$$

where

$$\begin{aligned} & \mathcal{A}(\mathbf{U}^l, \Phi^l)(\mathbf{w}, \psi - \Phi^l) \\ &:= \int_{\Lambda} (1-k)(E(\Phi^l)^2 + k)\sigma^+(\mathbf{U}^l) : e(\mathbf{w}) \, d\mathbf{x} + \int_{\Lambda} \sigma^-(\mathbf{U}^l) : e(\mathbf{w}) \, d\mathbf{x} \\ & \quad - \int_{\Lambda} (\alpha-1)E(\Phi^l)^2 P^l \nabla \cdot \mathbf{w} \, d\mathbf{x} + \int_{\Lambda} E(\Phi^l)^2 \nabla P^l \cdot \mathbf{w} \, d\mathbf{x} \\ & \quad + (1-k) \int_{\Lambda} \Phi^l \sigma^+(\mathbf{U}^l) : e(\mathbf{U}^l) \cdot (\psi - \Phi^l) \, d\mathbf{x} \\ & \quad - 2(\alpha-1) \int_{\Lambda} \Phi^l P^l \nabla \cdot \mathbf{U}^l \cdot (\psi - \Phi^l) \, d\mathbf{x} + \int_{\Lambda} 2\Phi^l \nabla P^l \cdot \mathbf{U}^l \cdot (\psi - \Phi^l) \, d\mathbf{x} \\ & \quad - G_c \int_{\Lambda} \frac{1}{\varepsilon} (1 - \Phi^l) \cdot (\psi - \Phi^l) \, d\mathbf{x} + G_c \int_{\Lambda} \varepsilon \nabla \Phi^l \cdot \nabla (\psi - \Phi^l) \, d\mathbf{x}. \end{aligned}$$

The solution of this nonlinear variational inequality is briefly explained in section 6 with all details presented in [41].

5.4. Level set and interpolation width. For the solution of the fracture pressure equation, we need the permeabilities, which depend on the fracture opening displacements. Based on the solution of Formulation 5, we are able to compute the

fracture opening displacements (width). We briefly recapitulate the main ideas in this section.

The spatially discretized solution variables for the level set and the width are denoted by $\Phi_{LS}(\mathbf{x}, t)$ and $W(\mathbf{x}, t)$, respectively. Those functions are approximated by using continuous piecewise polynomials given in their respective finite element spaces,

$$\mathbb{V}_{LS}(\mathcal{T}) := \{V_{LS} \in C^0(\bar{\Lambda}; \mathbb{R}) \mid V_{LS} = 0 \text{ on } \Gamma_F, V_{LS}|_{\mathcal{K}} \in \mathbb{Q}^1(\mathcal{K}), \forall \mathcal{K} \in \mathcal{T}\}$$

for the level set and

$$\mathbb{V}_w(\mathcal{T}) := \{V_w \in C^0(\bar{\Lambda}; \mathbb{R}) \mid V_w = 0 \text{ on } \partial\Lambda, V_w|_{\mathcal{K}} \in \mathbb{Q}^1(\mathcal{K}), \forall \mathcal{K} \in \mathcal{T}\}$$

for the width. After the computation of the displacement field $\mathbf{U}^{n,l}$ and the phase-field $\Phi^{n,l}$ at time t^n and iteration number l , the level set function introduced in (2.10) is simply computed as follows:

$$(5.7) \quad \Phi_{LS}^{n,l} = \Phi^{n,l} - C_{LS}.$$

Details of the entire procedure and different algorithms to consider the level set evaluation are provided in [56, 72]. As described in section 2.3, we compute the width W_D^l on the fracture boundary Γ_F by

$$(5.8) \quad 2W_D^l = -[\mathbf{U}^l \cdot \mathbf{n}_F] = -2\mathbf{U}^l \cdot \frac{\nabla\Phi_{LS}^l}{\|\nabla\Phi_{LS}^l\|}.$$

Remark 5.1. We recall for the convenience of the reader that our definition of the width W_D^l concerns only one-half of the fracture (see Figure 1). Thus, in order to get the full width, we need to multiply by the factor 2.

Finally, we interpolate the above computed width values W_D^l on Γ_F to values inside the fracture (see Remark 2.2), and denote the solution by W^l . Here, we briefly introduce the weak formulation for the interpolation process to solve for W^l as described in [56].

FORMULATION 6. *Find $W^l \in C^0([0, T]; \mathbb{V}_w(\mathcal{T}))$ such that*

$$\mathcal{A}_W(W^l, \psi) = \mathcal{F}_W(\psi) \quad \forall \psi \in \mathbb{V}_w(\mathcal{T}),$$

where

$$\begin{aligned} \mathcal{A}_W(W^l, \psi) &= (\nabla W^l, \nabla \psi) + \theta \int_{\Gamma_F^{n,l}} W^l \psi \, ds, \\ \mathcal{F}_W(\psi) &= \theta \int_{\Gamma_F^{n,l}} W_D^l \cdot \psi \, ds. \end{aligned}$$

5.5. Decomposing the domain Λ into Ω'_R , Ω'_F , and Ω'_e . Based on the previous two subsections, we have obtained \mathbf{U}^l , Φ^l , and W^l . Then¹ we increment $l \rightarrow l+1$; see Figure 4. We now address the coupling of flow and saturations between the fracture and the porous medium yielding P^{l+1} and S^{l+1} .

¹The reason why we ordered the subsections of section 5 in that way, having the pressure/saturations last, is that for the pressure equation we need the width from the displacements. On the other hand, the classical idea of the fixed-stress algorithm is to solve first for flow (pressures) and afterwards for geomechanics.

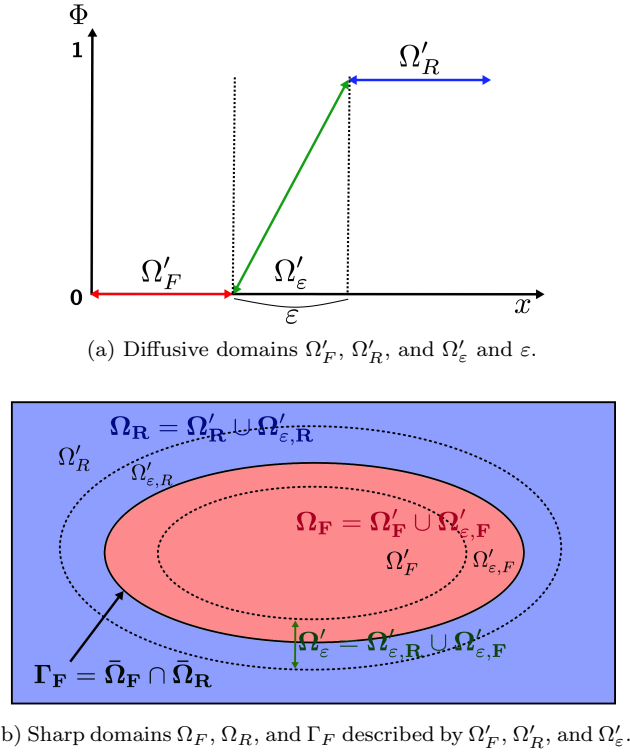


FIG. 5. Definitions for different domains are depicted with a phase-field variable. (a) Ω'_F , Ω'_R , and Ω'_ε , are considered as diffusive domains and defined, where $\Phi = 0$, $\Phi \in (0,1)$, and $\Phi = 1$, respectively. Ω_ε is the transition zone between Ω_F and Ω_R with the length ε . (b) Ω_F , Ω_R , and Γ_F are considered as sharp domains and interfaces. Relations between the sharp and diffusive domains are illustrated, i.e., $\Omega_F := \Omega'_F \cup \Omega'_{\varepsilon,F}$ and $\Omega_R := \Omega'_R \cup \Omega'_{\varepsilon,R}$. The red color indicates the sharp fracture zone.

A conceptional challenge is that we consider both diffusive and sharp interfaces. We assume a sharp interface for the pressure coupling and modeling but the phase-field fracture framework yields a diffusive (smeared) interface (see Figure 5). To this end, we partition the transition zone (Ω'_ε) into a fracture part ($\Omega'_{\varepsilon,F}$) and a porous medium part ($\Omega'_{\varepsilon,R}$), which we describe in this section. This decomposition is the basis for so-called diffraction systems in which the same type of equations is imposed on the entire domain, but the different parts (fracture and porous media) are distinguished by time-dependent and spatially varying coefficients.

First, we define the fracture domain Ω'_F and the reservoir domain Ω'_R by introducing the following two linear indicator functions χ_F and χ_R for the two different subdomains as

$$(5.9) \quad \chi_R := \chi_R(\Phi) = 1 \quad \text{in} \quad \Omega'_R(t) \quad \text{and} \quad \chi_R = 0 \quad \text{in} \quad \Omega'_F(t),$$

$$(5.10) \quad \chi_F := \chi_F(\Phi) = 1 \quad \text{in} \quad \Omega'_F(t), \quad \text{and} \quad \chi_F = 0 \quad \text{in} \quad \Omega'_R(t).$$

The transition zone Ω'_ε is characterized as follows:

$$\chi_R + \chi_F = 1 \quad \text{in} \quad \Omega'_\varepsilon,$$

where $\chi_R \neq 1$ and $\chi_F \neq 1$ and have intermediate values between 0 and 1.

By employing the already computed phase-field values $\Phi^{n,l}$ as an indicator function, we can specifically define

$$(5.11) \quad \chi_R^{n,l} := \frac{1 + H_h^*(\Phi^{n,l})}{2} \text{ and } \chi_F^{n,l} := \frac{1 - H_h^*(\Phi^{n,l})}{2},$$

where $H_h^*(.)$ is an approximation of the Heaviside function given as

$$(5.12) \quad H_h^*(w) = \begin{cases} 1 & \text{if } w > 0.5 + D_\epsilon, \\ -1 & \text{if } w < 0.5 - D_\epsilon, \\ \frac{w - 0.5}{D_\epsilon} & \text{otherwise.} \end{cases}$$

The transition zone Ω'_ϵ is characterized by the third case. Here, we set $D_\epsilon = 0.1$ as discussed in section 5.4.

5.6. Discretization of flow/pressure using EG. The EG space approximation $P(\mathbf{x}, t)$ of the pressure function is approximated by piecewise polynomials in the following finite element space:

$$(5.13) \quad \mathbb{V}_k^{EG} := \mathbb{M}_0^k(\mathcal{T}) + \mathbb{M}^0(\mathcal{T}),$$

where

$$(5.14) \quad \mathbb{M}^k(\mathcal{T}) := \{M \in L^2(\Lambda) | M|_{\mathcal{K}} \in \mathbb{Q}^k(\mathcal{K}), \forall \mathcal{K} \in \mathcal{T}\}$$

and

$$(5.15) \quad \mathbb{M}_0^k(\mathcal{T}) := \mathbb{M}^k(\mathcal{T}) \cap C(\Lambda).$$

The space $\mathbb{M}_0^k(\mathcal{T})$ is the subspace of $\mathbb{M}^k(\mathcal{T})$ consisting of the globally continuous piecewise continuous functions. Here we choose linear finite elements with $k = 1$; see [13, 49–51, 88] for more details.

Using section 5.5 and employing the phase-field as an indicator function, we can couple the two phase flow equations (3.61) in the fracture with the single phase equation (4.5) in the reservoir in terms of a pressure diffraction system. The following discretization is obtained using a standard derivation by multiplying the pressure diffraction system [52, 54, 68] by a discontinuous test function in \mathbb{V}_k^{EG} , integration by parts, and summing over elements .

We recall our notation introduced in section 5.2.1, namely, that $P^n := P_{F,\text{inj}}^n$ and $P^l := P^{n,l}$. We focus on the specifics of the fixed-stress iteration between flow and geomechanics/fracture as described in section 5.2. Then, the discretized problem reads as follows.

FORMULATION 7. At time t^n and the fixed-stress level $l + 1$, let $\mathbf{U}^l, \Phi^l, W^l, S^l$ be given. Furthermore, let the previous time step solutions U^{n-1}, P^{n-1} be given. We iterate for $l = 1, 2, 3, \dots$ such that find $P^{l+1} \in \mathbb{V}_1^{EG}$:

$$(5.16) \quad \mathcal{A}_P(P^{l+1}, \psi) = \mathcal{F}_P(\psi) \quad \forall \psi \in \mathbb{V}_1^{EG},$$

where the incomplete interior penalty Galerkin (IIPG) is employed to be compatible with the saturation system [28, 83]. Here the variational form is defined as

$$(5.17) \quad \mathcal{A}_P(P^{l+1}, \psi) := \sum_{\mathcal{K} \in \mathcal{T}} \int_{\mathcal{K}} \theta^l \frac{P^{l+1} - P^{n-1}}{\delta t} \psi \, d\mathbf{x} + \sum_{\mathcal{K} \in \mathcal{T}} \int_{\mathcal{K}} K_{\text{eff}}^l \nabla P^{l+1} \cdot \nabla \psi \, d\mathbf{x} \\ - \sum_{e \in \mathcal{E}_h^1} \int_e \{ K_{\text{eff}}^l \nabla P^{l+1} \} [\psi] \, d\gamma + \sum_{e \in \mathcal{E}_h^1} \int_e \frac{\alpha_p}{h_e} [P^{l+1}] [\psi] \, d\gamma,$$

where $\alpha_p > 0$ is a penalty parameter and the right-hand side is defined as

$$(5.18) \quad \mathcal{F}_P(\psi) := \sum_{\mathcal{K} \in \mathcal{T}} \int_{\mathcal{K}} q^l \psi \, d\mathbf{x} + \sum_{\mathcal{K} \in \mathcal{T}} \int_{\mathcal{K}} f^l \psi \, d\mathbf{x} \\ - \sum_{\mathcal{K} \in \mathcal{T}} \int_{\mathcal{K}} \theta_c^l \nabla P_c(S^l) \cdot \nabla \psi \, d\mathbf{x} + \sum_{e \in \mathcal{E}_h^1} \int_e \{ \theta_c^l \nabla P_c(S^l) \} [\psi] \, d\gamma.$$

Here the diffraction coefficients are defined as

$$(5.19) \quad \theta^l := \chi_R(\Phi^l) \left(\frac{1}{M_B} + \frac{3\alpha^2}{3\lambda + 2\mu} \right) + \chi_F(\Phi^l)(c_F),$$

$$(5.20) \quad K_{\text{eff}}^l := \chi_R(\Phi^l) \left(\frac{K_R}{\eta_R} \right) + \chi_F(\Phi^l) (K_F(W^l) \lambda_{tot}(S^l)),$$

$$(5.21) \quad q^l := \chi_R(\Phi^l) (q_R^n) + \chi_F(\Phi^l) (q_F)_{tot}^n,$$

$$(5.22) \quad f^l := \chi_R(\Phi^l) \left(\left(\frac{3\alpha^2}{3\lambda + 2\mu} \right) \left(\frac{P^l - P^{n-1}}{\delta t} \right) - \left(\alpha \nabla \cdot \left(\frac{\mathbf{U}^l - \mathbf{U}^{n-1}}{\delta t} \right) \right) \right) \\ + \chi_F(\Phi^l) \cdot 0,$$

$$(5.23) \quad \theta_c^l := \chi_R(\Phi^l) \cdot 0 + \chi_F(\Phi^l) (K_F(W^l) \lambda_{F,\text{res}}(S^l)).$$

Here we assume no flow boundary conditions on $\partial\Lambda$.

Remark 5.2. For the stability of the numerical solution, we have added (as it is very often done for such problems) the time derivative $\partial_t \chi_F(\Phi^l) c_F p$ in Formulation 7, which corresponds to assuming a slightly compressible fluid with the fracture fluid compressibility c_F .

Finally, for the saturation approximation in the next section, we introduce flux variables. Here, the conservative flux variables of the injected fluid in fractures, $\mathbf{V}^{l+1}(\mathbf{U}^l, W^l, S^l, P^{l+1})$, can be obtained as shown in [49, 51, 88]:

$$(5.24) \quad \mathbf{V}^{l+1}|_T := -K_{\text{eff}}^l \nabla P^{l+1} \quad \forall \mathcal{K} \in \mathcal{T},$$

$$(5.25) \quad \mathbf{V}^{l+1} \cdot \mathbf{n}|_e := -\{ K_{\text{eff}}^l \nabla P^{l+1} \} \cdot \mathbf{n} + h_e^{-1} [P^{l+1}] \quad \forall e \in \mathcal{E}_h^o,$$

where \mathbf{n} is the unit normal vector of the boundary edge e of \mathcal{K} .

5.7. Numerical discretization of saturation. In this subsection, we provide the EG approximation of the saturation Formulation 4 described in section 3.1.10. The space approximation of the injected saturation $s_{F,\text{inj}}(\cdot, t)$ is denoted by $S_{F,\text{inj}}(\mathbf{x}, t)$ using the same linear EG finite element space \mathbb{V}_1^{EG} as the pressure system. As shorthand notation, we denote the approximation of $S_{F,\text{inj}}(\mathbf{x}, t^n)$ by $S^n := S_{F,\text{inj}}^n$ and as before $S^l := S^{n,l}$. As for the pressure system, we formulate the saturation system in the spirit of a diffraction problem, despite the fact that the saturation is only present in the fracture in this work. However, this formalism allows us an easy extension to two phase flow in the reservoir once such a model shall be employed.

FORMULATION 8. Let the previous fixed-stress solutions $\mathbf{U}^l, \Phi^l, W^l, P^{l+1}$ and the previous time step solutions S^{n-1} be given. At time t^n we iterate for $l = 1, 2, 3, \dots$: Find $S^{l+1} \in \mathbb{V}_1^{EG}$ such that

$$(5.26) \quad \mathcal{A}_S(S^{l+1}, \psi) = \mathcal{F}_S(\psi) \quad \forall \psi \in \mathbb{V}_1^{EG},$$

where \mathcal{W} is the IHPG interior penalty method and the variational form is defined as

$$(5.27) \quad \begin{aligned} \mathcal{A}_S(S^{l+1}, \psi) := & \sum_{\mathcal{K} \in \mathcal{T}} \int_{\mathcal{K}} \theta_s^l \frac{S^{l+1} - S^{n-1}}{\delta t} \psi d\mathbf{x} + \sum_{\mathcal{K} \in \mathcal{T}} \int_{\mathcal{K}} \mu_{stab}^{l+1} \nabla S^{l+1} \cdot \nabla \psi d\mathbf{x} \\ & - \sum_{e \in \mathcal{E}_h^1} \int_e \{\!\{ \mu_{stab}^{l+1} \nabla S^{l+1} \}\!\} [\![\psi]\!] d\gamma + \sum_{e \in \mathcal{E}_h^1} \int_e \frac{\alpha_s}{h_e} \{\!\{ \mu_{stab}^{l+1} \}\!\}_{|e} [\![S^{l+1}]\!] [\![\psi]\!] d\gamma, \end{aligned}$$

where α_s is a penalty parameter. We note that terms weighted with μ_{stab}^{l+1} are artificial diffusion terms for numerical stabilization to ensure $s \in [0, 1]$ and which avoid spurious oscillations for the advection system. Then,

$$(5.28) \quad \mathcal{F}_S(\psi) := \sum_{\mathcal{K} \in \mathcal{T}} \int_{\mathcal{K}} \mathbf{V}^{l+1} \nabla \psi d\mathbf{x} - \sum_{e \in \mathcal{E}_h^1} \int_e \mathbf{V}^{l+1} \cdot \mathbf{n} [\![\psi]\!] d\gamma + \sum_{\mathcal{K} \in \mathcal{T}} \int_{\mathcal{K}} q_s^l \psi d\mathbf{x}.$$

The artificial viscosity is defined as

$$\mu_{stab}^{l+1} := c_s h_{\mathcal{K}} \|V^{l+1}\|_{L^\infty(\mathcal{K})},$$

where c_s is a positive constant. For more details, the readers are referred to [49]. Here the diffraction coefficients are defined as

$$(5.29) \quad \theta_s^l := \chi_R(\Phi^l) \cdot 0 + \chi_F(\Phi^l)(\phi_F^*),$$

$$(5.30) \quad q_s^l := \chi_R(\Phi^l) \cdot 0 + \chi_F(\Phi^l)(q_{F,inj}^n).$$

6. Parallel solvers and mesh adaptivity. We briefly discuss the numerical solvers to treat the discretized Formulations 5, 6, 7, 8. The overall problem is a large coupled framework in three dimensions which is treated by parallel computing and local mesh adaptivity in order to keep the computational costs reasonable.

We describe the solvers in the following with more details: Both, the pressure and saturation diffraction problems, are solved with generalized minimal residual method (GMRES) solvers with diagonal block-preconditioning. The nonlinear quasi-monolithic displacement/phase-field system presented in Formulation 5 is solved with Newton's method and line search algorithms. The constraint minimization problem is treated with a semismooth Newton method (i.e., a primal-dual active set method). Both methods are combined in one single loop leading to a robust and efficient iteration scheme that is outlined in [41]. Within Newton's loop we solve the linear equation systems with GMRES solvers with diagonal block-preconditioning from Trilinos [42]. Finally, the linear-elliptic level set and width problems are solved with a parallel CG solver and symmetric successive overrelaxation preconditioning.

To allow for small phase-field regularization parameters ε , we employ a predictor-corrector scheme that chooses an initial $\varepsilon > h_{\mathcal{K}}$ at the beginning of the computation [41]. Since this is a model parameter, we do not want to change the model during the computation and therefore keep ε fixed. However, the crack propagates and in coarse mesh regions $\varepsilon > h_{\mathcal{K}}$ may be violated. Then, we take the first step as a predictor step,

and refine the mesh such that $\varepsilon > h_K$ holds again and finally recompute the solution. It has been shown in [41] (2D) and [54, 97] (3D) that this procedure is efficient and robust. As a refinement criterion we simply take a threshold value of the phase-field variable, i.e., once $\Phi < C_A$ with $0 < C_A < 1$, e.g., $C_A \sim 0.8$, we flag a mesh element for refinement.

The implementation is done in our software IPACS (integrated parallel advanced crack simulator), which is an extension of [54, 97] based on the open-source MPI parallel phase-field fracture framework [41] using deal.II [12], p4est [20], and Trilinos [42].

7. Numerical examples. In this section, we present several numerical examples to substantiate our proposed algorithms and models.

7.1. Example 1: A fracture propagation in a homogeneous media. In this first example, we consider a single propagating fracture. A first fluid, the residing fluid, is already present. We then inject a second fluid.

This example is split into two subsections. In the first test (Example 1(a)), the crack is aligned with the x -axis and thus finally on existing mesh faces. In the second example (Example 1(b)) the initial crack is shifted by 45 degrees in order to show that phase-field fracture allows for arbitrary initial cracks, not necessarily aligned with the mesh, but leading to the same findings (same crack length, maximal pressure, etc.). This is a very important feature of phase-field fracture and shows that our entire derivation holds irrespectively of the initial geometric configuration.

Configuration. We deal with the following geometric data: $\Omega = (0 \text{ m}, 4 \text{ m})^2$ and a (prescribed) initial crack which has a half-length $l_0 = 0.2 \text{ m}$ on $\Omega_F = (1.8, 2.2) \times (2 - h_{\max}, 2 + h_{\max}) \subset \Omega$ (Example 1(a)) and shifted by 45 degrees in the middle of the domain at $(2 \text{ m}, 2 \text{ m})$ for Example 1(b). The initial mesh is 5 times uniformly refined. We then allow for three levels of predictor-corrector mesh refinement.

Boundary and initial conditions. For the displacements we prescribe homogeneous Dirichlet conditions on $\partial\Lambda$. For the phase-field and the pressure system, homogeneous Neumann conditions are employed. The boundary conditions for the crack-width problem have been explained in section 5.4. The initial phase-field values are set to zero for the initial fracture described above and $\varphi = 1$ otherwise. Also the initial displacement and pressure values are set to zero.

Parameters. The time step size is chosen as $\delta t = 0.01 \text{ s}$. The total number of time steps is 1000 with the final time 10 s . The phase-field value for the predictor-corrector refinement is chosen as 0.8; thus below 0.8 the mesh will be refined up to three times. The penalization parameter for the EG pressure system is set to 100. The penalization parameter for the saturation system is set to 1000. The capillary coefficient is $\gamma_{res} = 1$. Furthermore, $TOL_{FS} = 10^{-3}$ and the Newton tolerance for the phase-field displacement system is 10^{-10} .

The regularization parameters are chosen as $\varepsilon = 2h$ and $\kappa = 10^{-10}h$. Biot's coefficient is $\alpha = 1$. Furthermore the wellbore pressure is $q_F = 5 \text{ m}^3/\text{s}$ and $M_B = 1 \times 10^8 \text{ Pa}$, $c_F = 1 \times 10^{-8} \text{ Pa}$. The viscosities are chosen as $\nu_R = \nu_F = 1 \times 10^{-3} \text{ Ns/m}^2$. The reservoir permeability is $K_R = 1 \text{ d}$. The densities are $\rho_F^0 = 1 \text{ kg/m}^3$. The critical energy release rate is chosen as $G_c = 1 \times 10^3 \text{ N m}^{-1}$, Young's modulus is $E = 10^8 \text{ Pa}$, the Poisson ratio is set to $\nu = 0.2$. The relationship to the Lamé coefficients μ and λ is given by

$$\mu = \frac{E}{2(1+\nu)}, \quad \lambda = \frac{\nu E}{(1+\nu)(1-2\nu)}.$$

Observation goals. We observe the length of the fracture in terms of the phase-field variable, the predictor-corrector mesh refinement, the crack-width distribution, and the pressure and saturation distributions.

Discussion of our findings. In Figure 6, we observe the crack pattern and the predictor-corrector mesh refinement at three different times. The fracture width solution is displayed in Figure 7. Here we observe a smooth width field, which is parabolic with respect to the injection point. The largest width can be identified in the injection point. The pressure and saturation distributions are shown in Figure 8. Pressure is similar to our previous results. Namely, we observe negative pressure at the fracture tips and pressure dropping when the fracture starts propagating (see Figure 8). The saturation develops a slower than a priori expected. On the other hand, the material is fully saturated and the injecting fluid needs to push the existing fluid away, which requires a certain time.

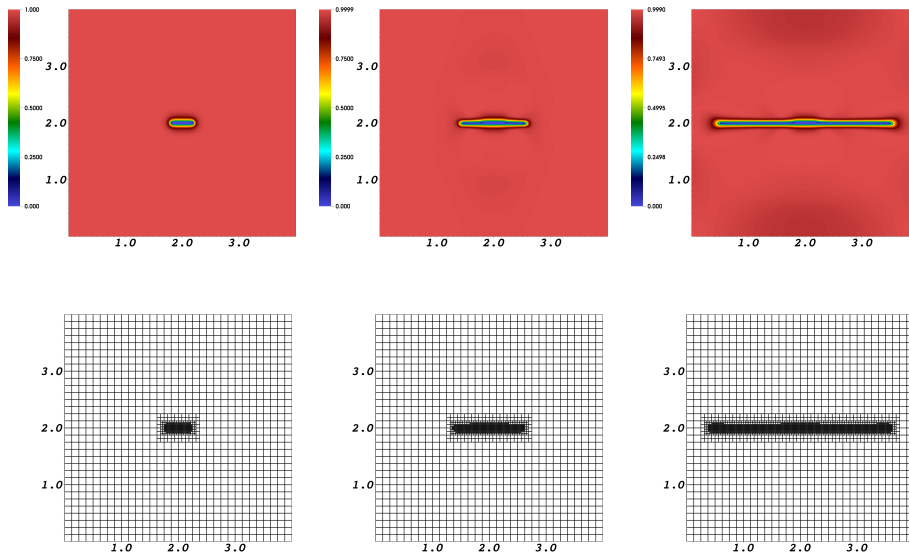


FIG. 6. Example 1(a): Fracture path displayed in terms of the phase-field variable on top. At the bottom the locally adapted mesh where the refinement criterion depends on the phase-field value at each cell. The visualizations are taken at $T = 0.01$ s, 2 s, 10 s.

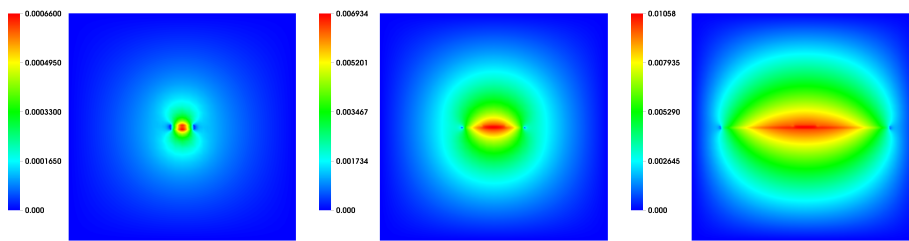


FIG. 7. Example 1(a): the fracture width at $T = 0.01$ s, 2 s, 10 s.

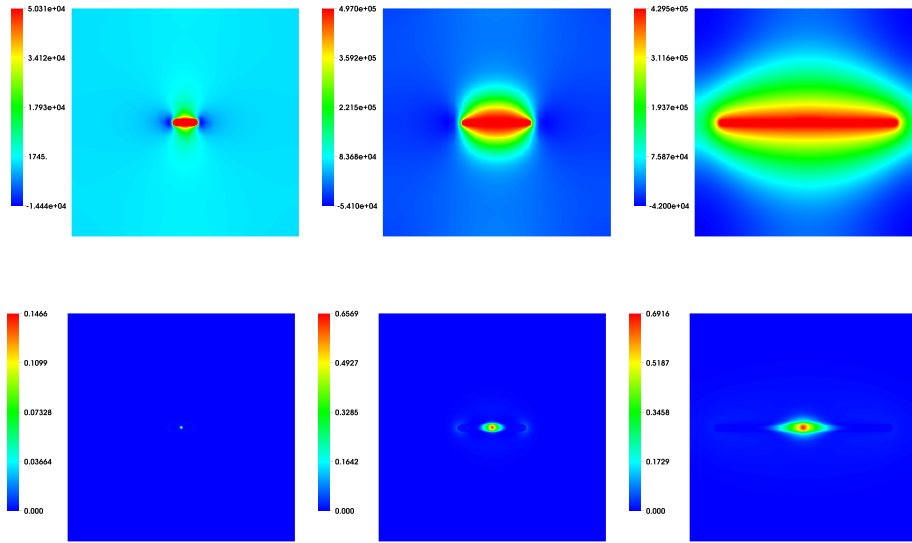


FIG. 8. Example 1(a): The pressure and saturation distributions at $T = 0.01$ s, 2 s, 10 s.

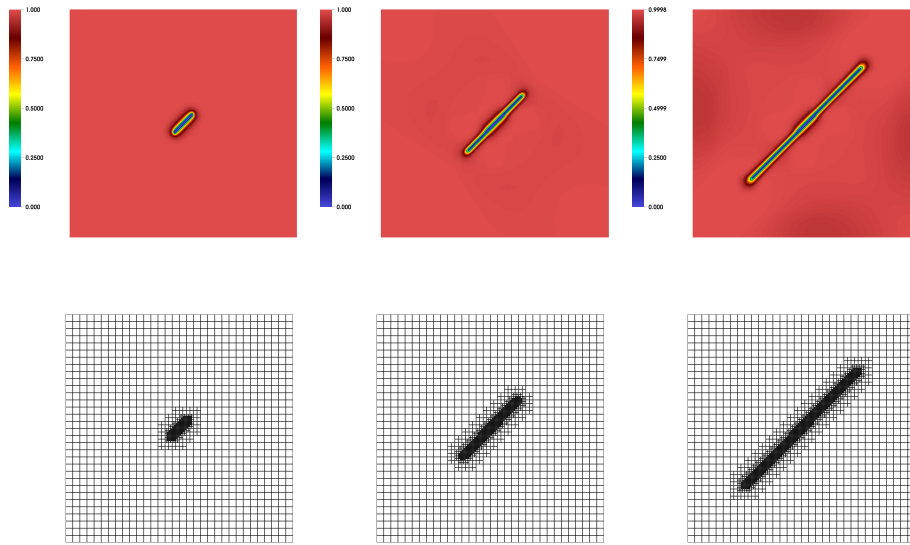
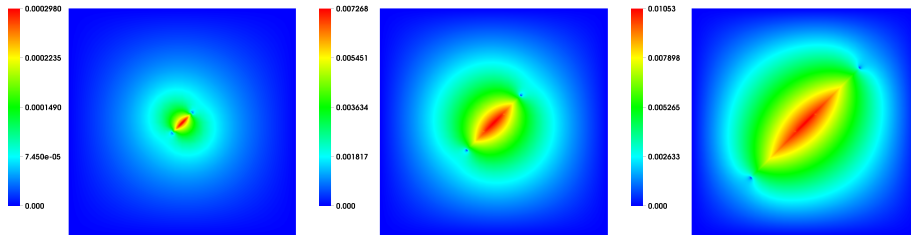
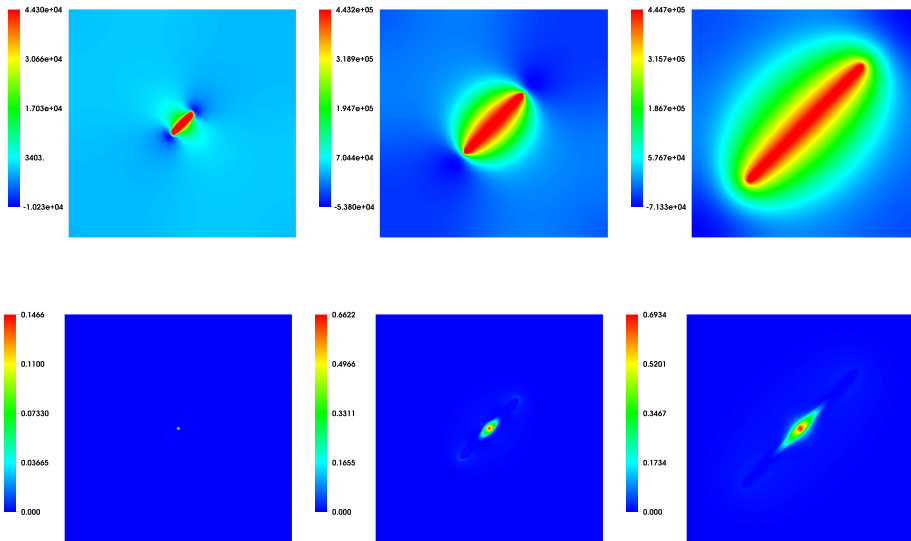


FIG. 9. Example 1(b): Fracture path displayed in terms of the phase-field variable on top. At the bottom the locally adapted mesh where the refinement criterion depends on the phase-field value at each cell. The visualizations are taken at $T = 0.01$ s, 2 s, 10 s.

We ran a second series of tests, referenced as Example 1(b). A common claim in phase-field studies is that the fracture is independent of the mesh and does not need to be aligned with mesh faces. In order to study this independence we shifted the initial fracture by 45 degrees. The results are displayed in Figures 9, 10, and 11. Here

FIG. 10. Example 1(b): The fracture width at $T = 0.01$ s, 2 s, 10 s.FIG. 11. Example 1(b): The pressure and saturation distributions at $T = 0.01$ s, 2 s, 10 s.

we indeed observe the same range of values for the width, pressure, and saturation as for the straight crack. The length of the fracture, displayed in Figure 9, corresponds to the straight crack length shown in Figure 6.

A quantitative comparison of the maximum pressure and the maximum crack width (crack opening displacement) is provided in Figure 12. While there are slight differences in the pressures, the width evolutions show excellent agreement for the straight and diagonal crack settings, respectively. We thus conclude that the model is independent with respect to the initial crack location, here a rotation.

With regard to the computational cost of the nonlinear solver for the displacement/phase-field system (details can be found in [41]) and fixed-stress iterations (see Figure 4 and Algorithm 1), we observe very similar iteration numbers in this example as recently published in [56, section 6.3]. Specifically we have on average about 5 Newton iterations per time step for solving Formulation 5. Fixed-stress iteration numbers are displayed in Figure 13, which are also very reasonable.

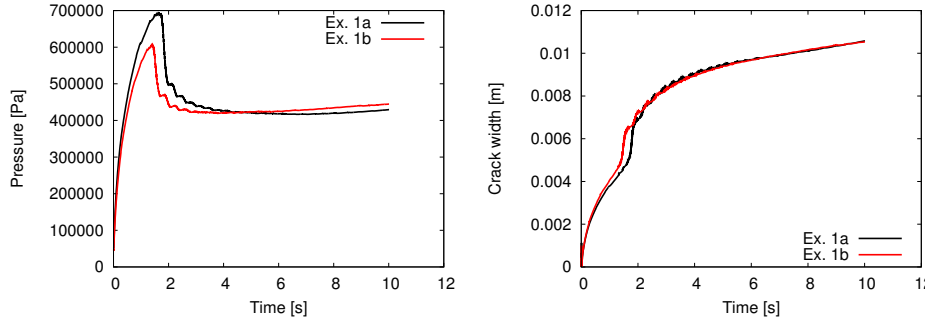


FIG. 12. Example 1: Quantitative comparison of the evolutions of the maximum pressure and the maximum crack width. At the highest pressures, the values differ by about 15% while the difference is about 3% at the end at $T = 10$ s. The crack width values also differ slightly, but by much less. From these data, we conclude a very good agreement and thus an independence of the model with respect to the geometry (i.e., here a rotation of the initial fracture). We expect the data to converge closer on finer meshes, which we may further quantify in future studies.

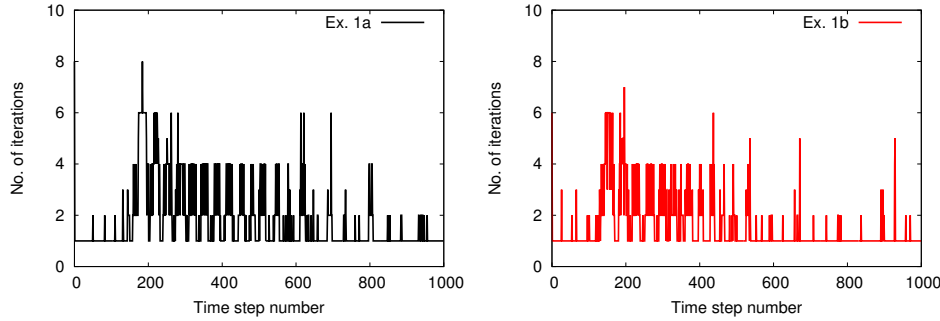


FIG. 13. Example 1: Fixed stress iteration numbers per time step for both fracture settings.

7.2. Example 2: Multiple fractures propagation in a heterogeneous media.

In this example, multiple parallel fractures are propagating with multiple injections.

Configuration. Here $\Omega := (0\text{m}, 4\text{m})^2$ and we prescribe three parallel initial cracks with half-lengths $l_0 = 0.2\text{ m}$ as illustrated in Figure 14. The initial mesh is locally refined an additional four times around the fracture (see Figure 14(b)).

Boundary and initial conditions. For the displacements we prescribe homogeneous Dirichlet conditions on $\partial\Lambda$. For the phase-field and the pressure system, homogeneous Neumann conditions are employed. The boundary conditions for the crack-width problem have been explained in section 5.4. The initial fractures are positioned at $(\beta - h_{\min}, \beta + h_{\min}) \times (2 - l_0, 2 + l_0)$, where $\beta = 0.75\text{ m}$, 2 m , and 3.25 m with the phase value set to zero. The initial displacement and pressure values are also set to zero.

Parameters. The smallest mesh size is $h_{\min} = 0.0055\text{ m}$ and the regularization parameters for the phase-field are chosen as $\varepsilon = 2h_{\min}$ and $\kappa = 10^{-10}h_{\min}$. In the homogeneous media, the critical energy release rate is chosen as $G_c = 10\text{ N m}^{-1}$, Young's modulus is $E = 10^8\text{ Pa}$, and the Poisson ratio is set to $\nu = 0.2$. For the fluid parameters, Biot's coefficient is set as $\alpha = 1$, $M_B = 1 \times 10^8\text{ Pa}$, $\eta_R = \eta_{F,\text{res}} = 3 \times 10^{-3}\text{ Ns/m}^2$, $\eta_{F,\text{inj}} = 1 \times 10^{-3}\text{ Ns/m}^2$, the reservoir permeability is $K_R =$

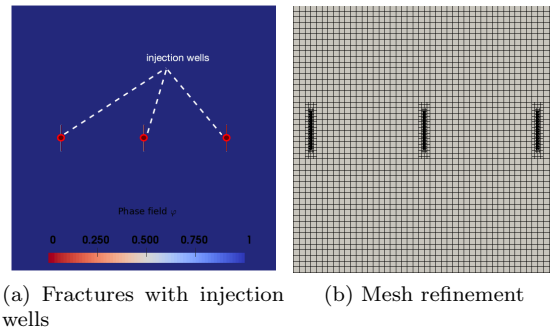
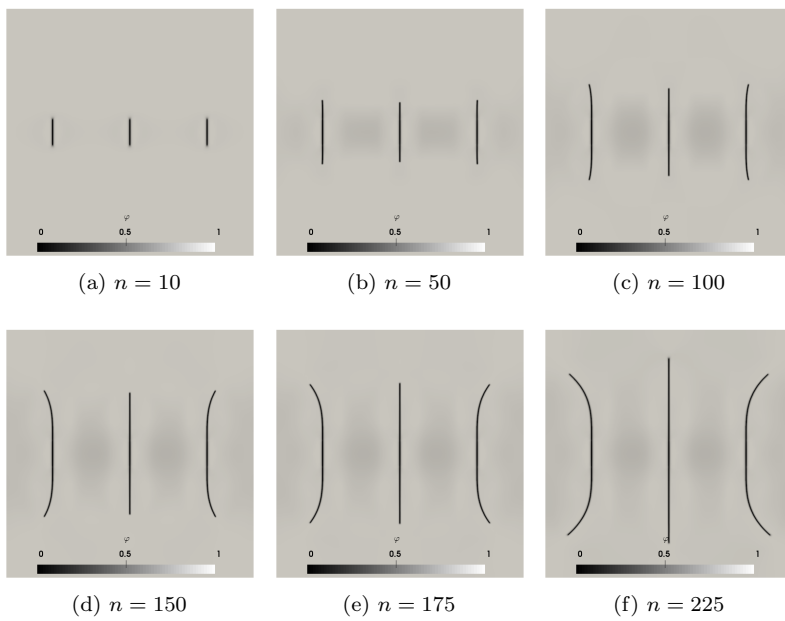


FIG. 14. Example 2: Setup

FIG. 15. Example 2: Phase-field fracture values for different time step numbers n .

$1D \approx 1 \times 10^{-12} \text{ m}^2$, $q_F = 10$, and $c_F = 1 \times 10^{-12} \text{ Pa}^{-1}$. The capillary pressure coefficients are $\gamma_{\text{res}} = 0.01$, $\theta = 0$, $\phi = 1$ for (3.50) and to avoid the singularity we use $p_c(S_\varepsilon)$, where $S_\varepsilon = 0.2$. The numerical parameters are set to $\alpha_p = 100$, $\alpha_s = 100$, and $c_s = 1$. The uniform time step size is $\delta t = 0.01$.

Observation goals. First, we observe the length of the fracture in terms of the phase-field variable and expect the stress shadowed effect [11, 47, 77] with close enough parallel fractures. Then, we plot the saturation distributions inside the fractures.

Discussion of our findings. Figure 15 illustrates the fracture propagation for different time steps with corresponding phase-field values. Injected fluid saturation $S_{F,\text{inj}}$ is presented in Figure 16. The stress shadowed effect is observed where the left and right fractures are curving out. The optimal distances between fractures to maximize propagated fracture surfaces and to avoid these effects with the phase-field model are discussed in [55].

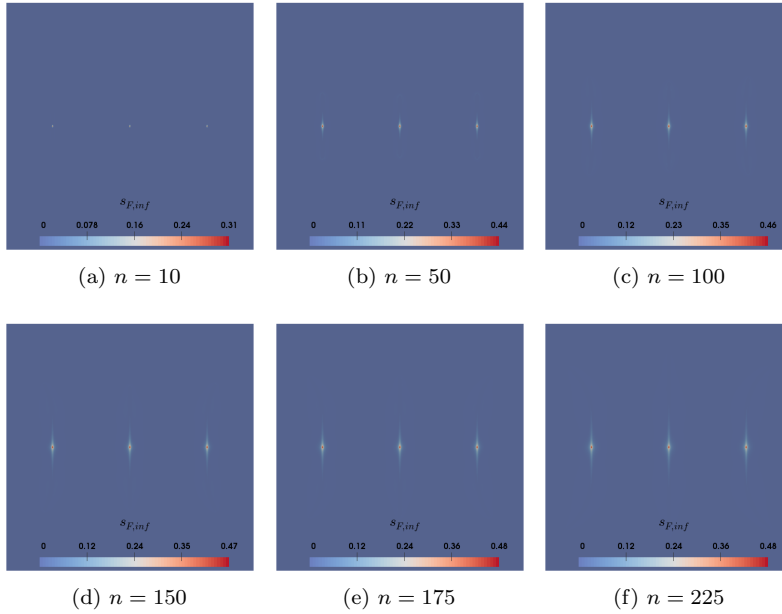


FIG. 16. Example 2: Injected fluid saturation values for different time step numbers n .

7.3. Example 3: A propagating penny-shaped fracture in a 3D homogeneous medium. In this final example, a penny-shaped fracture is propagating in a 3D domain. The idea of this setting is similar to Example 1 and most parameters are the same. From a coding perspective the extension from two dimensions to three dimensions is a major step, but relatively easy to accomplish in our code.

Configuration. The domain is a cube $\Omega = (0 \text{ m}, 4 \text{ m})^3$ and a (prescribed) initial penny-shaped crack with radius $l_0 = 0.25 \text{ m}$. The initial mesh is 2 times uniformly refined and we allow for an additional 5 levels of predictor-corrector mesh refinement. The boundary conditions are the same as in Example 1, but now in three dimensions. The initial conditions are similar to the 2D test cases: the initial phase-field value is 0 in the fracture and 1 outside. The remaining variables are initialized by zero values.

Parameters. The time step size is chosen as $\delta t = 0.01 \text{ s}$. The total number of time steps is 250 with the final time 2.5 s. The phase-field value for the predictor-corrector refinement is chosen as 0.8; thus, below 0.8 the mesh will be refined up to three times. The penalization parameter for the enriched Galerkin pressure system is set to 100. The penalization parameter for the saturation system is set to 1000. The capillary coefficient is $\gamma_{res} = 1$. Furthermore, $TOL_{FS} = 10^{-3}$ and the Newton tolerance for the phase-field displacement system is 10^{-10} .

The regularization parameters are chosen as $\varepsilon = 2h$ and $\kappa = 10^{-10}h$. Biot's coefficient is $\alpha = 1$. Furthermore the wellbore pressure is $q_F = 2 \text{ m}^3/\text{s}$ and $M_B = 1 \times 10^8 \text{ Pa}$, $c_F = 1 \times 10^{-8} \text{ Pa}$. The viscosities are chosen as $\nu_R = \nu_F = 1 \times 10^{-3} \text{ Ns/m}^2$. The reservoir permeability is $K_R = 1 \text{ d}$. The densities are $\rho_F^0 = 1 \text{ kg/m}^3$. The critical energy release rate is chosen as $G_c = 1 \times 10^3 \text{ N m}^{-1}$, Young's modulus is $E = 10^8 \text{ Pa}$, and the Poisson ratio is set to $\nu = 0.2$.

Observation goals. We observe the length of the fracture in terms of the phase-field variable, the predictor-corrector mesh refinement, the crack-width distribution, and the pressure and saturation distributions.

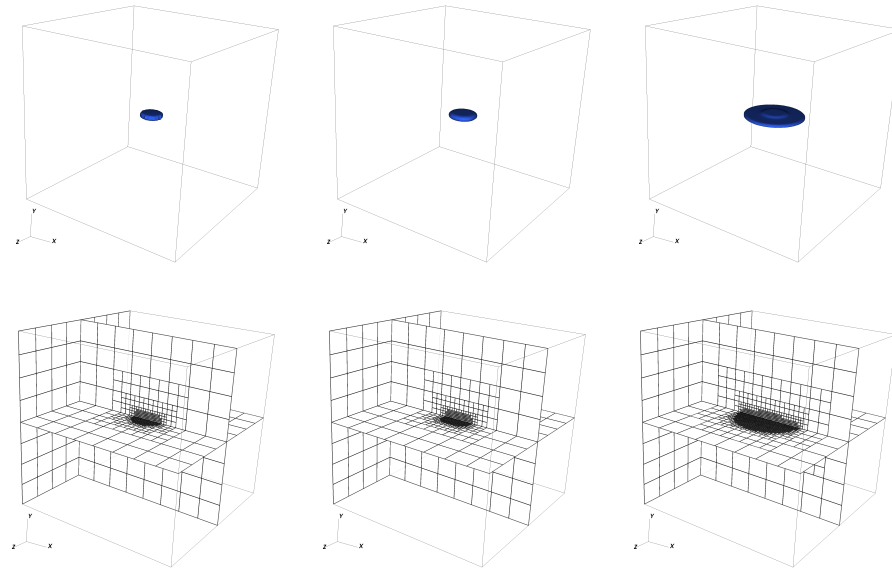


FIG. 17. Example 3: The fracture in terms of the phase-field variable and the locally refined mesh at $T = 0.01$ s, 1.25 s, 2.5 s.

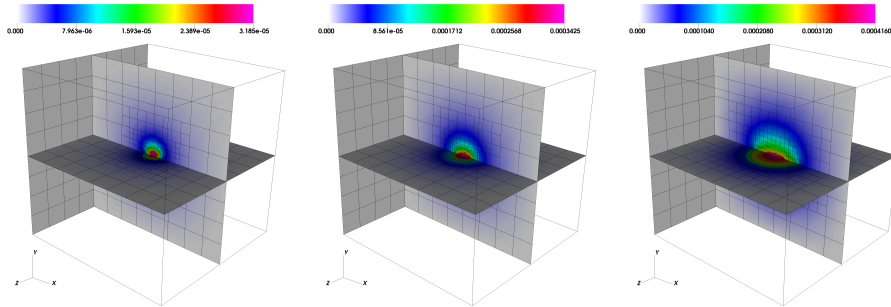


FIG. 18. Example 3: The fracture width at $T = 0.01$ s, 1.25 s, 2.5 s. The color scale is adjusted dynamically in each subfigure, i.e., rose/red colors display the highest width values at the current step. These maximal values are 3.185×10^{-5} , 3.425×10^{-4} , and 4.16×10^{-4} , respectively.

Discussion of our findings. Our findings are displayed in Figures 17, 18, and 19. We observe that the fracture propagates in a penny-shaped fashion and the mesh is locally refined with the predictor-corrector scheme. In particular in these three dimensional this procedure helps enormously to reduce the computational cost. In more detail, we start with a total number of 7792 at $T = 0.01$ s, over 8184 at $T = 1.25$ s, and ending with 23724 grid cells at $T = 2.5$ s.

The saturation (of the injecting fluid) propagates slower than the fracture itself, which we already observed for the 2D test cases. Our simulations confirm our modeling parts in which we assumed a radial injecting fluid.

8. Conclusion. In this paper, we proposed a model for immiscible two phase flow in a propagating fracture using a variational phase-field model. A residing fluid can be considered as oil whereas the injecting fluid may be considered to be water.

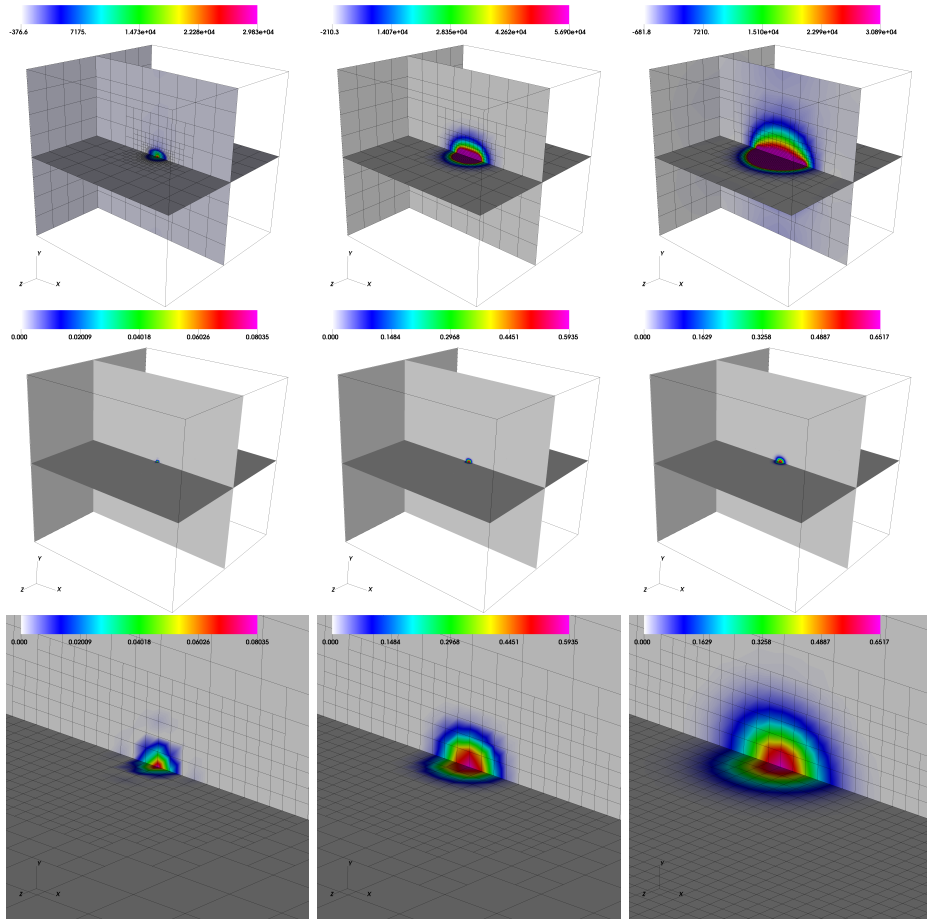


FIG. 19. Example 3: The pressure (first row) and saturation distributions (second row) at $T = 0.01$ s, 1.25 s, 2.5 s. In the last row a zoom-in of the saturation values is provided.

The flow model in the fracture is derived from multifluid Stokes equations, employing upscaling. The calculation is a natural extension of our previous work [52] and [68], where the lubrication approximation was used to calculate the permeability tensor for a single phase fluid flow through a penny-shaped fracture. In this paper, we have considered a thin penny-shaped fracture filled by two viscous incompressible fluids, separated by a free boundary. The wetting fluid was injected radially, while displacing the existing residing fluid. Using the approach from [64], the free boundary was described using a hyperbolic equation for the viscosity. Thus, the free boundary defines the saturation. We upscaled the multifluid Stokes equations to the Buckley–Leverett equations and calculated the absolute and relative permeabilities as functions of the saturations explicitly by using a two-scale expansion.

Moreover, we also account for capillary pressure. These quantities are then used in 3D equations for pressure and saturation in the fracture. Flow in the poroelastic medium is assumed to be of single phase. In order to obtain an accurate fracture width (i.e., jump of displacements across the fracture boundaries), we adopt a level-set approach and a finite element fracture width problem. The next challenging part is the coupling of the two phase flow system with single phase flow on the fracture

boundary. Here we employ diffraction systems with varying coefficients in space and time. These developments result in a four-field problem: pressure, saturation, phase-field-displacements, and fracture width.

In order to ensure conservation properties of the continuous system, we develop specifically tailored discretization schemes. For the phase-field displacement and crack-width systems, standard continuous finite element methods are employed. The numerical discretization of pressure and saturation ask for local mass conservation. These are ensured by using an enriched Galerkin scheme. In order to keep the computational cost reasonable, we implemented local mesh adaptivity that allows for small phase-field regularization parameters in the fracture zone and an MPI-parallelized framework.

While the pressure, saturation, and fracture width systems are linear and can be solved directly with iterative solvers, the phase-field displacement system is nonlinear and respects a crack irreversibility condition. Here, we use a combined semismooth Newton solver based on a primal-dual active set strategy. In the final section, we present three prototype test cases that show the capabilities of the presented modeling and computational frameworks.

While this is a first study with detailed modeling and specifically tailored construction of numerical discretization schemes, future work will be focusing on further treating more practical field problems.

Acknowledgments. T. Wick thanks his former host institution Centre de Mathématiques Appliquées at École Polytechnique (France) for providing support and resources in preparing this paper.

REFERENCES

- [1] EIA ANNUAL ENERGY OUTLOOK 2017, u. s. Energy Information Administration.
- [2] J. ADACHI, E. SIEBRITS, A. PEIRCE, AND J. DESROCHES, *Computer simulation of hydraulic fractures*, Int. J. Rock Mech. Mining Sci., 44 (2007), pp. 739–757.
- [3] T. ALMANI, S. LEE, M. F. WHEELER, AND T. WICK, *Multirate Coupling for Flow and Geomechanics Applied to Hydraulic Fracturing Using an Adaptive Phase-Field Technique*, Technical report SPE-182610-MS. Society of Petroleum Engineers, Richardson, TX, 2017.
- [4] M. AMBATI, T. Gerasimov, AND L. DE LORENZIS, *A review on phase-field models of brittle fracture and a new fast hybrid formulation*, Comput. Mech., 55 (2015), pp. 383–405.
- [5] L. AMBROSIO AND V. TORTORELLI, *Approximation of functionals depending on jumps by elliptic functionals via γ -convergence*, Comm. Pure Appl. Math., 43 (1990), pp. 999–1036.
- [6] L. AMBROSIO AND V. TORTORELLI, *On the approximation of free discontinuity problems*, Boll. Unione Mat. Ital. B, 6 (1992), pp. 105–123.
- [7] H. AMOR, J.-J. MARIGO, AND C. MAURINI, *Regularized formulation of the variational brittle fracture with unilateral contact: Numerical experiments*, J. Mech. Phys. Solids, 57 (2009), pp. 1209–1229.
- [8] T. ARBOGAST, M. JUNTUNEN, J. POOL, AND M. F. WHEELER, *A discontinuous Galerkin method for two-phase flow in a porous medium enforcing $H(\text{div})$ velocity and continuous capillary pressure*, Comput. Geosci., 17 (2013), pp. 1055–1078.
- [9] K. AZIZ AND A. SETTARI, *Petroleum Reservoir Simulation*, Applied Science, London, 1979.
- [10] A. BABCHIN AND B. FAYBISHENKO, *On the capillary pressure function in porous media based on relative permeabilities of two immiscible fluids*, Colloids Surfaces A, 462 (2014), pp. 225–230.
- [11] T. BAI, D. D. POLLARD, AND H. GAO, *Explanation for fracture spacing in layered materials*, Nature, 403 (2000), pp. 753–756.
- [12] W. BANGERTH, D. DAVYDOV, T. HEISTER, L. HELTAI, G. KANSCHAT, M. KRONBICHLER, M. MAIER, B. TURCKSIN, AND D. WELLS, *The deal.II library, version 8.4*. J. Numer. Math., 24, (2016), pp. 135–142.
- [13] R. BECKER, E. BURMAN, P. HANSBO, AND M. G. LARSON, *A reduced P1-Discontinuous Galerkin Method*, Technieal report, 2003-13, Chalmers Finite Element Center Chalmers University of Technology, Gothenburg, Sweden, 2003.

- [14] M. J. BORDEN, C. V. VERHOOSSEL, M. A. SCOTT, T. J. R. HUGHES, AND C. M. LANDIS, *A phase-field description of dynamic brittle fracture*, Comput. Meth. Appl. Mech. Engrg., 217 (2012), pp. 77–95.
- [15] B. BOURDIN, *Numerical implementation of the variational formulation for quasi-static brittle fracture*, Interfaces Free Bound., 9 (2007), pp. 411–430.
- [16] B. BOURDIN, G. FRANCFOR, AND J.-J. MARIGO, *Numerical experiments in revisited brittle fracture*, J. Mech. Phys. Solids, 48 (2000), pp. 797–826.
- [17] B. BOURDIN, C. CHUKWUDZIE, AND K. YOSHIOKA, *A Variational Approach to the Numerical Simulation of Hydraulic Fracturing*, SPE-159154-MS, Richardson, TX, 2012.
- [18] B. BOURDIN, J.-J. MARIGO, C. MAURINI, AND P. SICSIĆ, *Morphogenesis and propagation of complex cracks induced by thermal shocks*, Phys. Rev. Lett., 112 (2004), 014301.
- [19] A. BOURGEAT, E. MARUŠIĆ-PALOKA, AND A. MIKELIĆ, *Effective fluid flow in a porous medium containing a thin fissure*, Asymptot. Anal., 11 (1995), pp. 241–262.
- [20] C. BURSTEDDE, L. C. WILCOX, AND O. GHATTAS, *P4est: Scalable algorithms for parallel adaptive mesh refinement on forests of octrees*, SIAM J. Sci. Comput., 33 (2011), pp. 1103–1133.
- [21] T. CAJUHI, L. SANAVIA, AND L. DE LORENZIS, *Phase-field modeling of fracture in variably saturated porous media*, Comput. Mech., 61 (2017), pp. 299–318.
- [22] N. CASTELLETTO, J. A. WHITE, AND H. A. TCHELEPI, *Accuracy and convergence properties of the fixed-stress iterative solution of two-way coupled poromechanics*, Int. J. Numer. Anal. Methods Geomech., 39 (2015), pp. 1593–1618.
- [23] G. CHAVENT AND J. JAFFRÉ, *Mathematical Models and Finite Elements for Reservoir Simulation: Single Phase, Multiphase and Multicomponent Flows through Porous Media*, stud. Math. Appl. Eng. 17. Elsevier, Amsterdam, 1986.
- [24] Z. CHEN, G. HUAN, AND Y. MA, *Computational methods for multiphase flows in porous media*, Comput. Sci. Eng. 2, SIAM, Philadelphia, 2006.
- [25] P. CONCUS AND W. PROSKUROWSKI, *Numerical solution of a nonlinear hyperbolic equation by the random choice method*, J. Comput. Phys., 30 (1979), pp. 153–166.
- [26] L. CUETO-FELGUEROSO AND R. JUANES, *A phase-field model of two-phase Hele-Shaw flow*, J. Fluid Mech., 758 (2014), pp. 522–552.
- [27] B. DAMJANAC AND P. CUNDALL, *Application of distinct element methods to simulation of hydraulic fracturing in naturally fractured reservoirs*, Comput. Geotech., 71 (2016), pp. 283–294.
- [28] C. DAWSON, S. SUN, AND M. WHEELER, *Compatible algorithms for coupled flow and transport*, Comput. Methods Appl. Mech. Engrg., 193 (2004), pp. 2565–2580.
- [29] D. A. DiCARLO, *Experimental measurements of saturation overshoot on infiltration*, Water Res. Res., 40 (2004), 2003 WR002670.
- [30] E. DONTSOV AND A. PEIRCE, *A multiscale implicit level set algorithm (ILSA) to model hydraulic fracture propagation incorporating combined viscous, toughness, and leak-off asymptotics*, Comput. Methods Appl. Mech. Engrg., 313 (2017), pp. 53–84.
- [31] M. J. ECONOMIDES, AND K. G. NOLTE, *Reservoir Stimulation*, Wiley, New York, 2000.
- [32] M. F. EL-AMIN, J. KOU, S. SUN, AND A. SALAMA, *An iterative implicit scheme for nanoparticles transport with two-phase flow in porous media*, Procedia Comput. Sci., 80 (2016), pp. 1344–1353.
- [33] ENERGYFROMSHALE., *What is Fracking?*, www.what-is-fracking.com/what-is-hydraulic-fracturing/.
- [34] M. FOURAR AND S. BORIES, *Experimental study of air-water two-phase flow through a fracture (narrow channel)*, Int. J. Multiph. Flow, 21 (1995), pp. 621–637.
- [35] M. FOURAR, AND R. LENORMAND, *A viscous coupling model for relative permeabilities in fractures* SPE-49006-MS in SPE Annual Technical Conference and Exhibition, New Orleans, Louisiana, Society of Petroleum Engineers, Richardson, TX, 1998, pp. 27–30.
- [36] G. FRANCFOR AND J.-J. MARIGO, *Revisiting brittle fracture as an energy minimization problem*, J. Mech. Phys. Solids, 46 (1998), pp. 1319–1342.
- [37] E. GORDELIY AND A. PEIRCE, *Coupling schemes for modeling hydraulic fracture propagation using the XFEM*, Comput. Methods Appl. Mech. Engrg., 253 (2013), pp. 305–322.
- [38] P. GUPTA AND C. DUARTE, *Simulation of non-planar three-dimensional hydraulic fracture propagation*, Int. J. Numer. Anal. Methods Geomech., 38 (2014), pp. 1397–1430.
- [39] P. GUPTA AND C. DUARTE, *Coupled hydromechanical-fracture simulations of nonplanar three-dimensional hydraulic fracture propagation*, Int. J. Numer. Anal. Methods Geomech., 42 (2018), pp. 143–180.
- [40] Y. HEIDER AND B. MARKERT, *A phase-field modeling approach of hydraulic fracture in saturated porous media*, Mech. Res. Comm., 80 (2017), pp. 38–46.

- [41] T. HEISTER, M. F. WHEELER, AND T. WICK, *A primal-dual active set method and predictor-corrector mesh adaptivity for computing fracture propagation using a phase-field approach*, Comput. Methods Appl. Mech. Engrg., 290 (2015), pp. 466–495.
- [42] M. HEROUX, R. BARTLETT, V. H. R. HOEKSTRA, J. HU, T. KOLDA, R. LEHOUCQ, K. LONG, R. PAWLOWSKI, E. PHIPPS, A. SALINGER, H. THORNQUIST, R. TUMINARO, J. WILLENBRING, AND A. WILLIAMS, *An Overview of Trilinos*, Technical Report SAND2003-2927, Sandia National Laboratories, Albuquerque, NM, 2003.
- [43] H. HOTEIT AND A. FIROOZABADI, *Numerical modeling of two-phase flow in heterogeneous permeable media with different capillarity pressures*, Adv. Water Res., 31 (2008), pp. 56–73.
- [44] J. KIM, H. TCHELEPI, AND R. JUANES, *Stability, accuracy, and efficiency of sequentiel methods for flow and geomechanics*, SPE Journal, 16 (2011), pp. 249–262.
- [45] J. KIM, H. TCHELEPI, AND R. JUANES, *Stability and convergence of sequentiel methods for coupled flow and geomechanics: Fixed-stress and fixed-strain splits*, Comput. Methods Appl. Mech. Engrg., 200 (2011), pp. 1591–1606.
- [46] Y. KOVALYSHEN, *Fluid-Driven Fracture in Poroelastic Medium*, Ph.D. thesis, The University of Minnesota, Minneapolis, MN, 2010.
- [47] A. H. LACHENBRUCH, *Depth and spacing of tension cracks*, J. Geophys. Res., 66 (1961), pp. 4273–4292.
- [48] B. LECAMPION, A. BUNGER, AND X. ZHANG, *Numerical methods for hydraulic fracture propagation: A review of recent trends*, J. Nat. Gas Sci. Eng., 49 (2018), pp. 66–83.
- [49] S. LEE AND M. F. WHEELER, *Enriched Galerkin methods for two-phase flow in porous media with capillary pressure*, J. Comput. Phys., 367 (2018), pp. 65–86.
- [50] S. LEE AND M. F. WHEELER, *Adaptive enriched Galerkin methods for miscible displacement problems with entropy residual stabilization*, J. Comput. Phys., 331 (2017), pp. 19–37.
- [51] S. LEE, Y.-J. LEE, AND M. F. WHEELER, *A locally conservative enriched Galerkin approximation and efficient solver for elliptic and parabolic problems*, SIAM J. Sci. Comput., 38 (2016), pp. A1404–A1429.
- [52] S. LEE, A. MIKELIĆ, M. F. WHEELER, AND T. WICK, *Phase-field modeling of proppant-filled fractures in a poroelastic medium*, Comput. Methods Appl. Mech. Engrg., 312 (2016), pp. 509–541.
- [53] S. LEE, J. E. REBER, N. W. HAYMAN, AND M. F. WHEELER, *Investigation of wing crack formation with a combined phase-field and experimental approach*, Geophys. Res. Lett., 43 (2016), pp. 7946–7952.
- [54] S. LEE, M. F. WHEELER, AND T. WICK, *Pressure and fluid-driven fracture propagation in porous media using an adaptive finite element phase field model*, Comput. Methods in Appl. Mech. and Eng., 305 (2016), pp. 111–132.
- [55] S. LEE, B. MIN, AND M. F. WHEELER, *Optimal design of hydraulic fracturing in porous media using the phase field fracture model coupled with genetic algorithm*, Comput. Geosci., 22 (2018), pp. 833–849.
- [56] S. LEE, M. F. WHEELER, AND T. WICK, *Iterative coupling of flow, geomechanics and adaptive phase-field fracture including level-set crack width approaches*, J. Comput. Appl. Math., 314 (2017), pp. 40–60.
- [57] S. LEE, M. F. WHEELER, T. WICK, AND S. SRINIVASAN, *Initialization of phase-field fracture propagation in porous media using probability maps of fracture networks*, Mech. Res. Comm., 80 (2017), pp. 16–23.
- [58] B. MARKERT AND Y. HEIDER, *Coupled multi-field continuum methods for porous media fracture*, in Recent Trends in Computational Engineering-CE2014, Springer, Cham, Switzerland, 2015, pp. 167–180.
- [59] M. W. MCCLURE, AND C. A. KANG, *A three-dimensional reservoir, wellbore, and hydraulic fracturing simulator that is compositional and thermal, tracks proppant and water solute transport, includes non-Darcy and non-Newtonian flow, and handles fracture closure*, in SPE Reservoir Simulation Conference, Society of Petroleum Engineers, Montgomery, TX, 2017.
- [60] C. MIEHE AND S. MAUTHE, *Phase field modeling of fracture in multi-physics problems. part III. Crack driving forces in hydro-poro-elasticity and hydraulic fracturing of fluid-saturated porous media*, Comput. Methods Appl. Mech. Engrg., 304 (2016), pp. 619–655.
- [61] C. MIEHE, M. HOFACKER, L.-M. SCHÄNZEL, AND F. ALDAKHEEL, *Phase field modeling of fracture in multi-physics problems. Part II. Coupled brittle-to-ductile failure criteria and crack propagation in thermo-elastic-plastic solids*, Comput. Methods Appl. Mech. Engrg., 294 (2015), pp. 486–522.
- [62] C. MIEHE, S. MAUTHE, AND S. TEICHTMEISTER, *Minimization principles for the coupled problem of Darcy Biot-type fluid transport in porous media linked to phase field modeling of fracture*, J. Mech. Phys. Solids, 82 (2015), pp. 186–217.

- [63] C. MIEHE, L.-M. SCHAENZEL, AND H. ULMER, *Phase field modeling of fracture in multi-physics problems. Part I. Balance of crack surface and failure criteria for brittle crack propagation in thermo-elastic solids*, Comput. Methods Appl. Mech. Engineering, 294 (2015), pp. 449–485.
- [64] A. MIKELIĆ AND L. PAOLI, *On the derivation of the Buckley–Leverett model from the two fluid Navier–Stokes equations in a thin domain* Comput. Geosci. 1 (1997), pp. 59–83, Comput. Geosci., 4 (2000), pp. 99–101.
- [65] A. MIKELIĆ AND M. F. WHEELER, *Convergence of iterative coupling for coupled flow and geomechanics*, Comput Geosci., 17 (2012), pp. 455–462.
- [66] A. MIKELIĆ, B. WANG, AND M. F. WHEELER, *Numerical convergence study of iterative coupling for coupled flow and geomechanics*, Comput. Geosci., 18 (2014), pp. 325–341.
- [67] A. MIKELIĆ, M. WHEELER, AND T. WICK, *Phase-Field Modeling of Pressurized Fractures in a Poroelastic Medium*, Technical report ICES Report 14-18, University of Texas at Austin, Austin, TX, 2014.
- [68] A. MIKELIĆ, M. F. WHEELER, AND T. WICK, *A phase-field method for propagating fluid-filled fractures coupled to a surrounding porous medium*, SIAM Multiscale Model. Simul., 13 (2015), pp. 367–398.
- [69] A. MIKELIĆ, M. F. WHEELER, AND T. WICK, *A quasi-static phase-field approach to pressurized fractures*, Nonlinearity, 28 (2015), pp. 1371–1399.
- [70] A. MIKELIĆ, M. F. WHEELER, AND T. WICK, *Phase-field modeling of a fluid-driven fracture in a poroelastic medium*, Comput. Geosci., 19 (2015), pp. 1171–1195.
- [71] T. MOHAMMADNEJAD AND A. KHOEI, *An extended finite element method for hydraulic fracture propagation in deformable porous media with the cohesive crack model*, Finite Elem. Anal. Des., 73 (2013), pp. 77–95.
- [72] T. NGUYEN, J. YVONNET, Q.-Z. ZHU, M. BORNERT, AND C. CHATEAU, *A phase-field method for computational modeling of interfacial damage interacting with crack propagation in realistic microstructures obtained by microtomography*, Comput. Methods Appl. Mech. Engrg., 312 (2016), pp. 567–595.
- [73] J. H. NORBECK, M. W. MCCLURE, J. W. LO, AND R. N. HORNE, *An embedded fracture modeling framework for simulation of hydraulic fracturing and shear stimulation*, Comput. Geosci., 20 (2016), pp. 1–18.
- [74] R. NORDGREN, *Propagation of a vertical hydraulic fracture*, SPE J., 12 (1972), pp. 306–314.
- [75] A. NOURI AND F. POUPAUD, *An existence theorem for the multi-fluid Navier–Stokes problem*, J. Differential Equations, 122 (1995), pp. 71–88.
- [76] A. NOURI, F. POUPAUD, AND Y. DEMAY, *An existence theorem for the multi-fluid Stokes problem*, Quart. Appl. Math., 55 (1997), pp. 421–435.
- [77] J. E. OLSON, *Predicting fracture swarms—the influence of subcritical crack growth and the crack-tip process zone on joint spacing in rock*, Geological Society, London, Special Publications, 231 (2004), pp. 73–88.
- [78] H. OUCHI, A. KATIYAR, J. YORK, J. T. FOSTER, AND M. M. SHARMA, *A fully coupled porous flow and geomechanics model for fluid driven cracks: A peridynamics approach*, Comput. Mech., 55 (2015), pp. 561–576.
- [79] L. PAOLI, *Asymptotic behavior of a two fluid flow in a thin domain: From Stokes equations to Buckley–Leverett equation and Reynolds law*, Asymptot. Anal., 34 (2003), pp. 93–120.
- [80] D. PEACEMAN, *Fundamentals of Numerical Reservoir Simulation*, Developments in Petroleum Science. Elsevier, Amsterdam, 2000.
- [81] T. PERKINS, AND L. KERN, *Widths of hydraulic fractures*, J. Petrol. Techno., 13 (1961), pp. 937–949.
- [82] J. RUTQVIST, Y.-S. WU, C.-F. TSANG, AND G. BODVARSSON, *A modeling approach for analysis of coupled multiphase fluid flow, heat transfer, and deformation in fractured porous rock*, Int. J. Rock Mech. Mining Sci., 39 (2002), pp. 429–442.
- [83] G. SCOVAZZI, M. F. WHEELER, A. MIKELIĆ, AND S. LEE, *Analytical and variational numerical methods for unstable miscible displacement flows in porous media*, J. Comput. Phys., 335 (2017), pp. 444–496.
- [84] A. SETTARI AND F. MOURITS, *A coupled reservoir and geomechanical simulation system*, SPE J., 3 (1998), pp. 219–226.
- [85] A. SETTARI AND D. A. WALTERS, *Advances in coupled geomechanical and reservoir modeling with applications to reservoir compaction*, SPE J., 6 (2001), pp. 334–342.
- [86] F. SHI, X. WANG, C. LIU, H. LIU, AND H. WU, *A coupled extended finite element approach for modeling hydraulic fracturing in consideration of proppant*, J. Nat. Gas Sci. Eng., 33 (2016), pp. 885–897.
- [87] I. N. SNEDDON AND M. LOWENGRUB, *Crack Problems in the Classical Theory of Elasticity*, SIAM Ser. in Appl. Math., Wiley, Philadelphia, 1969.

- [88] S. SUN AND J. LIU, *A locally conservative finite element method based on piecewise constant enrichment of the continuous Galerkin method*, SIAM J. Sci. Comput., 31 (2009), pp. 2528–2548.
- [89] S. SUN AND M. F. WHEELER, *Projections of velocity data for the compatibility with transport*, Comput. Methods Appl. Mech. Engrg., 195 (2006), pp. 653–673.
- [90] A. Z. SZERI, *Fluid film lubrication*, Cambridge University Press, Cambridge, 2010.
- [91] R. TEMAM, *Navier-Stokes Equations: Theory and Numerical Analysis*, AMS, Providence, RI, 2001.
- [92] C. J. VAN DUIJN, L. A. PELETIER, AND I. S. POP, *A new class of entropy solutions of the Buckley-Leverett equation*, SIAM J. Math. Anal., 39 (2007), pp. 507–536.
- [93] H. J. WELGE, *A simplified method for computing oil recovery by gas or water drive*, J. Petrol. Technol., 4 (1952), pp. 91–98.
- [94] M. F. WHEELER, T. WICK, AND W. WOLLNER, *An augmented-Lagrangian method for the phase-field approach for pressurized fractures*, Comput. Meth. Appl. Mech. Engrg., 271 (2014), pp. 69–85.
- [95] T. WICK, *Coupling fluid-structure interaction with phase-field fracture*, J. Comput. Phys., 327 (2016), pp. 67–96.
- [96] T. WICK, *An error-oriented Newton/inexact augmented Lagrangian approach for fully monolithic phase-field fracture propagation*, SIAM J. Sci. Comput., 39 (2017), pp. B589–B617.
- [97] T. WICK, S. LEE, AND M. F. WHEELER, *3D phase-field for pressurized fracture propagation in heterogeneous media*, VI International Conference on Computational Methods for Coupled Problems in Science and Engineering 2015 Proceedings, International Center for Numerical Methods in Engineering, Barcelona, 2015, pp. 605–613.
- [98] T. WICK, G. SINGH, AND M. WHEELER, *Fluid-filled fracture propagation using a phase-field approach and coupling to a reservoir simulator*, SPE J., 21 (2016), pp. 981–999.
- [99] P. A. WITHERSPOON, J. S. Y. WANG, K. IWAI, AND J. E. GALE, *Validity of cubic law for fluid flow in a deformable rock fracture*, Water Res. Res., 16 (1980), pp. 1016–1024.
- [100] Y. P. ZHELTOV AND S. KHRISTIANOVICH, *On hydraulic fracturing of an oil-bearing stratum*, Izv. Akad. Nauk SSSR. Otdel Tekhn. Nauk, 5 (1955), 41.
- [101] R. W. ZIMMERMAN AND G. S. BODVARSSON, *Hydraulic conductivity of rock fractures*, Transp. Porous Media, 23 (1996), pp. 1–30.